Orographically Modified Ice-Phase Precipitation Processes During the Olympic Mountains Experiment (OLYMPEX)

Andrew DeLaFrance[a], Lynn McMurdie[a], and Angela Rowe[b]

[a]*Department of Atmospheric Sciences, University of Washington, Seattle, Washington*

[b]*Department of Atmospheric and Oceanic Sciences, University of Wisconsin-Madison, Madison, Wisconsin*

Submitted to Journal of the Atmospheric Sciences

March 2021

Revised July 2021

Revised September 2021

Corresponding author: Andrew DeLaFrance, adelaf@uw.edu

Early Online Release: This preliminary version has been accepted for publication in *Journal of the Atmospheric Sciences*, may be fully cited, and has been assigned DOI 10.1175/JAS-D-21-0091.1. The final typeset copyedited article will replace the EOR at the above DOI when it is published.

ABSTRACT

Over mountainous terrain, windward enhancement of stratiform precipitation results from a combination of warm-rain and ice-phase processes. In this study, ice-phase precipitation processes are investigated within frontal systems during the Olympic Mountains Experiment (OLYMPEX). An enhanced layer of radar reflectivity (Z_H) above the melting level bright band (i.e., a secondary Z_H maximum) is observed over both the windward slopes of the Olympic Mountains and the upstream ocean, with a higher frequency of occurrence and higher Z_H values over the windward slopes indicating an orographic enhancement of ice-phase precipitation processes. Aircraft-based in situ observations are evaluated for the 01-02 and 03 December 2015 orographically-enhanced precipitation events. Above the secondary Z_H maximum, the hydrometeors are primarily horizontally oriented dendritic and branched crystals. Within the secondary Z_H maximum, there are high concentrations of large (> ~2 mm diameter) dendrites, plates, and aggregates thereof, with a significant degree of riming. In both events, aggregation and riming appear to be enhanced within a turbulent layer near sheared flow at the top of a low-level jet impinging on the terrain and forced to rise above the melting level. Based on windward ground sites at low-, mid-, and high-elevations, secondary Z_H maxima periods during all of OLYMPEX are associated with increased rain rates and larger mass-weighted mean drop diameters compared to periods without a secondary Z_H maximum. This result suggests that precipitation originating from secondary Z_H maxima layers may contribute to enhanced windward precipitation accumulations through the formation of large, dense particles that accelerate fallout.

Accepted for publication in *Journal of the Atmospheric Sciences*. DOI 10.1175/JAS-D-21-0091.1.

SIGNIFICANCE STATEMENT

Precipitation processes are modified within winter storms passing over the Olympic Mountains, often resulting in increased rain and snow on the windward slopes. This study evaluates precipitation characteristics and inferred growth processes related to radar reflectivity maxima within ice layers of clouds, providing insights into ice-phase contributions to windward precipitation. Ground- and aircraft-based measurements indicate that rapid ice growth may occur when branched and plate-like crystals are aggregated within turbulent regions that are prevalent over the windward slopes. Large aggregate particles gain mass by collection of supercooled liquid water which may increase precipitation fallout. While ground measurements suggest that ice-phase growth contributes to windward accumulations, some uncertainty about the processes that occur between the ice layer and the ground remain.

Accepted for publication in *Journal of the Atmospheric Sciences*. DOI10.1175/JAS-D-21-0091.1.

1. Introduction

Wintertime rain and snow accumulation in mountainous regions provides a necessary freshwater resource to neighboring lowland areas (Viviroli et al. 2007). Often, mountains receive enhanced precipitation accumulations on the windward slopes and diminished precipitation on the lee slopes (Smith 1979; Roe 2005; Houze 2012). When wintertime midlatitude cyclones encounter mountains, the windward enhancement of stratiform precipitation results from a complex combination of warm-rain processes below the melting level and ice-phase processes above (White et al. 2003; Kingsmill et al. 2006; Massmann et al. 2017; Zagrodnik et al. 2018, 2019). Ice particle growth occurs by diffusion (deposition), collection of other ice particles (aggregation), or accretion of supercooled liquid water drops (riming). Ice particle properties vary due to growth contributions from each process which has implications for the distribution of precipitation along windward and lee slopes of a mountain. Riming- and aggregation-dominated ice growth permits rapid fallout of precipitation on the windward slopes whereas precipitation is advected downstream in a slower depositional growth regime (Hobbs et al. 1973; Colle and Zeng 2004; Colle et al. 2005). A need for additional observational studies of these processes has been demonstrated by increasingly sophisticated approaches to model the microphysics of ice particle growth (Brdar and Seifert 2018; Grabowski et al. 2019).

Hydrometeor properties and growth processes are often inferred from dual-polarization radar measurements. Differential reflectivity, Z_{DR}, is the logarithmic difference between radar reflectivity factors at horizontal and vertical polarizations, Z_H and Z_V, with near-zero dB values for spherical or randomly oriented hydrometeors and increasing Z_{DR} for decreasing aspect ratio and preferentially horizontally oriented hydrometeors. Enhanced layers of positive Z_{DR} above the melting level near -15°C temperatures have consistently been linked to depositional growth of

Accepted for publication in *Journal of the Atmospheric Sciences*. DOI 10.1175/JAS-D-21-0091.1.

dendritic or plate-like ice crystals (e.g., Kennedy and Rutledge 2011; Andrić et al. 2013; Bechini et al. 2013; Schrom et al. 2015). Below these enhanced Z_{DR} layers, concurrently decreasing Z_{DR} and increasing Z_H is an indication of aggregation as particles increase in size and diversity of shape or orientation while falling toward the ground. Radar-based inferences of enhanced dendritic growth with active aggregation have been associated with heavy snowfall rates at the surface (Kennedy and Rutledge 2011; Kumjian and Lombardo 2017). However, polarimetric signatures aloft during winter storms may not be fully explained by dendritic and aggregational growth processes alone (Andrić et al. 2013), and the effects of secondary ice production and riming need to be considered. Indeed, Schrom et al. (2015) describe uncertainty in polarimetric radar signatures associated with the degree of riming and called for additional in situ measurements of particle types and size distributions coincident with radar observations to provide validation of radar-inferred microphysics.

Over complex terrain, several radar-based studies have considered whether orographically modified flow enhances, or at least alters, microphysical growth processes and the accompanying radar signatures aloft (e.g., Houze and Medina 2005; Kingsmill et al. 2006; Medina et al. 2007; McMurdie et al. 2018). Using vertically pointing S-band radar data in the northern California coastal mountains, Kingsmill et al. (2006) documented a pronounced increase in the rate of change in Z_H with height at about 2.5 km above the melting level that was termed a "shoulder". The “shoulder” occurred near -15°C temperatures and was considered a radar signature of accelerated hydrometeor growth rates, likely by aggregation. Below the “shoulder”, by definition, the rate of increase in Z_H toward the ground decreases and in some cases Z_H begins to decrease resulting in a local maximum in Z_H. They hypothesized that slower diffusional growth rates at warmer temperatures or a decrease in aggregation efficiency could

Accepted for publication in *Journal of the Atmospheric Sciences*. DOI 10.1175/JAS-D-21-0091.1.

explain this decrease in Z_H below the maximum. Kingsmill et al. (2006) proposed that because the "shoulder" was identified both at a mountainous site and at a downstream location, described as free from orographic influences, it was unlikely an orographically-forced response, but rather inherent to the large-scale environment.

In contrast, Medina et al. (2007) argued that a secondary Z_H maximum above the melting level is likely an orographically forced response or is at least enhanced by flow encountering topography. From a scanning S-band radar, they identified a secondary Z_H maximum at a height of approximately 3.5 to 5.5 km over the windward slopes of the Oregon Cascade Range (~1 to 2.5 km above the melting level) but not upstream, suggesting an orographic response in Z_H aloft. This finding is consistent with McMurdie et al. (2018) where a greater frequency of larger Z_H values occurred at all heights between 2 to 8 km over the windward slopes of the Olympic Mountains in Washington State when compared to upstream. The most significant enhancement of Z_H over the windward slopes occurred at a height of 4 to 6 km, comparable to the secondary Z_H maximum identified by Medina et al. (2007) and thus bolstering the suggestion of an orographic response aloft.

The physical processes associated with the secondary Z_H maximum in orographically modified flow are not well understood. In orographic studies that identified a secondary Z_H maximum (Houze and Medina 2005; Kingsmill et al. 2006; Medina et al. 2007; Zagrodnik et al. 2018; McMurdie et al. 2018), polarimetric radar measurements were either not considered or not available. Additionally, while polarimetric radar observations provide significant insight to ice growth processes, in situ measurements are ultimately necessary to validate or refute any radar-based inferences (e.g., Andrić et al. 2013; Schrom et al. 2015; Griffin et al. 2018).

Accepted for publication in *Journal of the Atmospheric Sciences*. DOI 10.1175/JAS-D-21-0091.1.

The 2015/16 Olympic Mountains Experiment (OLYMPEX) obtained radar-, aircraft-, and surface-based observations of midlatitude cyclones encountering the Olympic Mountains of Washington State, providing a rich dataset for investigating the orographic effects on ice-phase precipitation processes (Houze et al. 2017; Petersen et al. 2018). An S-band dual-polarization scanning radar collected observations upstream and over the windward slopes of the Olympic Mountains during two intensive observing periods (IOPs): 12 November to 19 December 2015 and 4-15 January 2016. In situ observations were collected within the radar domain by the University of North Dakota (UND) Citation aircraft during the first IOP. The purpose of this study is to use dual-polarization radar and in situ measurements to evaluate the microphysical properties of hydrometeors associated with secondary Z_H maxima and connect these observations to windward surface precipitation measurements to better understand the effects of orographically-modified ice microphysics on windward precipitation. In this study, OLYMPEX data are used to address the following questions:

1. Is a secondary Z_H maximum a signature of orographically modified ice-phase precipitation processes or is it solely a microphysical signature inherent to midlatitude frontal systems?
2. What hydrometeor properties and growth processes produce the secondary Z_H maximum?
3. How is the windward distribution and intensity of precipitation at the surface impacted by hydrometeor growth processes aloft?

2. Data

a. OLYMPEX Radar Data

Accepted for publication in *Journal of the Atmospheric Sciences*. DOI10.1175/JAS-D-21-0091.1.

NASA's S-band dual-polarization Doppler radar (NPOL) scanned nearly uninterrupted during OLYMPEX at a coastal site with an elevation of 139 m on the Olympic Peninsula (Fig. 1). NPOL's scanning strategy included a series of Range Height Indicator (RHI) scans extending to 45° in elevation at 3° azimuthal spacing from 210° to 326° over the ocean and at 2° azimuthal spacing from 30° to 60°, broadly covering the Quinault River Valley. The NPOL RHIs extended in range to 150 km with a 125-m gate spacing and 0.94° beamwidth. RHIs over a given location repeated every 20 minutes for a total of 2,113 complete radar scan cycles. This study uses version 2 of the NPOL data (Wolff et al. 2017) including calibrated Z_H and bias-corrected Z_{DR} (Wolff et al. 2015; Pippitt et al. 2015). For computational efficiency and simplification of the methods used to evaluate NPOL measurements, these data were interpolated to Cartesian coordinates using the Radx2Grid algorithm included in the Lidar Radar Open Software Environment (Bell et al. 2020). Data were gridded at 500-m horizontal and 250-m vertical grid spacing. NPOL data for this analysis is limited to a 60 km maximum range to reduce beam broadening impacts on polarimetric measurements (e.g., Sánchez-Diezma et al. 2000; Brandes and Ikeda 2004; Ryzhkov 2007; Giangrande et al. 2008) and to a minimum range of 10 km to include the full echo depth; echo tops during OLYMPEX rarely extended much higher than 8 km. In this study, we make comparisons between secondary Z_H maximum properties over the upstream ocean and the terrain by using detection methods defined by areal fraction thresholds. For these comparisons to be weighted fairly, the larger ocean-based RHI sector was divided into four 30° sectors of equal size to the terrain-focused sector: southwest (210°-240°), west-southwest (240°-270°), west-northwest (270°-300°), and approximately northwest (296°-326°). Because NPOL RHI scans over the northwest sector terminated at 326°, this sector overlaps with the west-northwest sector by four degrees. The southwest sector directly opposes the northeast

Accepted for publication in *Journal of the Atmospheric Sciences*. DOI 10.1175/JAS-D-21-0091.1.

(30°-60°), terrain-focused scan. The radar sector construction along cardinal orientations permit evaluation based on orientation upstream of the terrain. This approach was motivated by results from McMurdie et al. (2018) which described a pronounced increase in reflectivity values aloft over the terrain during periods of southwesterly low-level flow.

b. OLYMPEX Ground-Based Data

During OLYMPEX, the windward slopes of the Olympic Mountains were instrumented with Particle Size and Velocity 2 (Parsivel^2, Petersen et al. 2017a) disdrometers spanning from near the coast to an elevation of about 1600 m. Drop size distributions constructed from Parsivel^2 data in 2-minute segments were used to calculate rain rate and mass-weighted mean drop diameter following Zagrodnik et al. (2018). Although this method applies quality control measures to remove contamination of frozen precipitation, we have also removed any period in which the radar bright band was within 500 m of the ground site elevation. Three Parsivel^2 ground sites are used in this study to exhibit the change in orographic enhancement of precipitation with elevation (Fig. 1). The Fishery site is in the lower Quinault River Valley at an elevation of 51.8 m, at a distance of 19 km (~61° azimuth) from the NPOL site. Prairie Creek is a mid-elevation site at 542.5 m and 33.5 km distance (~39° azimuth) from NPOL. The Wynoochee site is in the high terrain at 1,018 m and 53.6 km distance (~62° azimuth) from NPOL.

Data used to describe atmospheric conditions were obtained from rawinsondes launched at the NPOL site typically every six hours but as frequently as three hours during storm events (Rutledge et al. 2018). Three-hourly North American Regional Reanalysis (NARR, Mesinger et al. 2006) data at the 32-km horizontal resolution grid point containing the NPOL location is used to fill in the temporal gaps of the soundings. Following McMurdie et al. (2018) and Zagrodnik et

Accepted for publication in *Journal of the Atmospheric Sciences*. DOI 10.1175/JAS-D-21-0091.1.

al. (2018), integrated water vapor transport (IVT) was used to describe the synoptic-scale moisture flux, 925-hPa wind as an indicator of the low-level flow pattern, and the moist static stability parameter, N_m^2 (Durran and Klemp 1982), as a measurement of atmospheric stability in three categories: moist unstable ($N_m^2 < -0.25 \times 10^{-4}\ s^{-2}$), moist neutral ($-0.25 \times 10^{-4}\ s^{-2} < N_m^2 < 0.25 \times 10^{-4}\ s^{-2}$), and moist stable ($N_m^2 > 0.25 \times 10^{-4}\ s^{-2}$). McMurdie et al. (2018) showed that the 925-hPa wind, N_m^2, and IVT values of the NARR dataset suitably characterize the synoptic environment during OLYMPEX.

c. OLYMPEX Aircraft Data

During the first IOP, the UND Citation flew primarily within the NPOL domain over the windward slopes and was equipped with microphysics probes to collect in situ measurements of cloud particles (Poellot et al. 2017). Measurements of two-dimensional projected ice particle images from two optical array probes (OAPs) were used to construct particle size distributions (PSDs) within the ice layer. We use the vertical channel of the 2D Stereo (2D-S) probe and the vertically-oriented High Volume Precipitation Spectrometer Version 3 (HVPS-3) probe. The University of Illinois/Oklahoma Optical Array Probe Processing Software (UIOOPS, McFarquhar et al. 2018) was used to process the 2D-S and HVPS-3 probe measurements. Following Chase et al. (2018) the 2D-S probe measurements were used for particles 0.225 to 1 mm in diameter, and the HVPS-3 probe measurements for particles 1 to 32.5 mm in diameter. The lower threshold of 0.225 mm in the 2D-S measurements minimizes inclusion of supercooled liquid water drops (Chase et al. 2018). UIOOPS defines particle diameter, D, by the minimum enclosing circle. The two-dimensional projected particle size observed from a fixed-orientation probe is an estimation of the particle's actual maximum dimension (e.g., Petty and Huang 2011).

Accepted for publication in *Journal of the Atmospheric Sciences*. DOI 10.1175/JAS-D-21-0091.1.

Neglecting any disturbance of the natural particle orientation by the aircraft, sampling of particles that fall with their long axis in a preferentially horizontal orientation with respect to vertically oriented probes means that D approximates the maximum particle dimension.

The spectral ice water content (IWC) is given as

$$IWC(D) = N(D)m(D), \quad (1)$$

where N(D) is the number concentration and m(D) is the particle mass at a given D. Reflectivity estimates derived from spectral IWC at size bins, j, following Hogan et al. (2006) are given as

$$Z_{PSD} = \frac{|K_i|^2}{0.93}\left(\frac{6}{\pi\rho_i}\right)^2 \sum_j m(D_j)^2 N(D_j) dD_j. \quad (2)$$

This method relies on the assumption of spherical particles and Rayleigh scattering properties. Calculations of spectral IWC require that a mass-dimension relationship be defined. Mass-dimension relationships from Brown and Francis (1995), Baker and Lawson (2006), Heymsfield et al. (2004), and a habit-specific relationship of the UIOOPS algorithm were evaluated by comparing Z_H measured from NPOL to Z_{PSD} calculated from in situ observations that were collected inside a grid cell within 60 seconds of the radar sampling time. Although a mass-dimension relationship must be established, we do not compute a total IWC for evaluation. Rather, we prioritize a mass-dimension relationship that provides the best fit for the measurement of primary interest, radar reflectivity, which is a higher-order moment of the PSD than IWC. For the two case studies in section 4b, the power-law relationship, $m = 0.0061D^{2.05}$, of Heymsfield et al. (2004) provided the best agreement with the NPOL radar having root mean square errors of 5.96 and 8.50 dB and absolute errors of -0.27 and -1.40 dB during the 01-02 December and 03 December events, respectively.

Accepted for publication in *Journal of the Atmospheric Sciences*. DOI 10.1175/JAS-D-21-0091.1.

Objective ice habit classification techniques in UIOOPS were applied to OAP imagery to better understand the microphysical contributions from unique particle habits. Habit classification includes nine ice habit classes: aggregate, dendrite, hexagonal, graupel, spherical, linear, oriented, irregular, and tiny following the algorithm of Holroyd (1987) which was optimized for the 2D-C OAP with a resolution of 25 μm. Our habit-specific analysis focuses largely on the HVPS-3 OAP imagery. Although the thresholds of the algorithm were not explicitly optimized to work with the coarse resolution of the HVPS-3 OAP (150 μm), manual evaluation of several subsets of habit-classified particles indicated that the UIOOPS algorithm generally classified particles from HVPS-3 images as expected. Nonetheless, we have limited our analysis of habit-classified ice particles using HVPS-3 imagery to a qualitative assessment only.

Two of the Citation's instruments are used to indicate supercooled liquid water. The King hot wire probe uses the power required to evaporate the liquid drops from a constant-temperature hot wire to derive liquid water content (LWC) estimates (King et al. 1978). A minimum threshold of 0.05 g m^{-3} is used to ensure measurements are indeed liquid water content and not an artifact of sensor noise. The Rosemount Icing Detector (RICE) was used to indicate the presence of supercooled liquid water. Although it is possible for it to be used to derive LWC estimates, the RICE instrument is most effective in discriminating mixed phase from glaciated clouds based on fixed thresholds (Cober et al. 2001) and will be used to support conclusions based on measurements from the King probe. All in situ measurements from the Citation probes used in this study were collected at 1 Hz sampling frequency.

3. Methods

Accepted for publication in *Journal of the Atmospheric Sciences*. DOI 10.1175/JAS-D-21-0091.1.

a. Bright Band Detection

An automated bright band detection algorithm was developed for the NPOL radar data. The bright band typically contains the 0°C level, thus providing segregation of stratiform and convective precipitation and a vertical partition of ice microphysics aloft from warm-rain processes below. At the melting level, reflectivity increases and copolar correlation coefficient, ρ_{HV}, the correlation of the horizontal and vertical radar pulses, decreases from a value of one due to increased diversity of hydrometeor shape, orientation, and phase (e.g., melting). Based on these principles, the bright band detection algorithm uses a grid-by-grid search procedure broadly adapted from methods of Gourley and Calvert (2003) and Giangrande et al. (2008) and modified to suit NPOL observations during OLYMPEX. The search procedure is performed independently for each radar sector shown in Fig. 1 as follows:

1. At each horizontal grid point the height of the column-minimum in ρ_{HV} is identified, if one exists between values of 0.91 and 0.97. From all grid points in a radar sector, the most frequently occurring (mode) vertical level of ρ_{HV} minima is identified.
2. Within 500 m below to 1000 m above the ρ_{HV} minimum mode level, individual grid-point bright bands are identified as the height of the column-maximum Z_H if it exceeds 25 dBZ (Fig. 2a).
3. If the number of individual grid points that have a bright band, N_{BB}, is more than 35% of the total grid points in the radar sector, individual grid-point bright band heights are averaged to produce a mean bright band height for that radar sector. For radar scan cycles having N_{BB} fewer than 35% of the sector's total grid points, no bright band is identified.

Accepted for publication in *Journal of the Atmospheric Sciences*. DOI 10.1175/JAS-D-21-0091.1.

295 The ρ_{HV} constraint is used to minimize the influence of high Z_H values within embedded
296 convective elements or from ground clutter, ensuring that our bright band height is mostly
297 representative of stratiform melting of ice hydrometeors. An asymmetric vertical search window
298 about the ρ_{HV} minimum is used because the minimum in ρ_{HV} commonly occurs below the Z_H
299 maximum at the bright band (Brandes and Ikeda 2004). There is an exemption that allows the
300 use of the second most commonly occurring ρ_{HV} minima mode level when it occurs below 4 km,
301 is at a higher elevation than the first, and has a mean layer Z_H exceeding 15 dBZ. This exemption
302 was useful in a small number of radar scan cycles where the melting level is either very deep or
303 close to the surface resulting in low ρ_{HV} values from ground clutter. We have removed time
304 periods with a bright band height greater than 500 m above or below a rolling mean of ten
305 consecutive bright band heights to minimize the inclusion of embedded convective elements.
306 Depending on the radar sector, this resulted in one to nine scan cycles (~20-minute periods)
307 removed.

308 Bright band detection is based on three primary input thresholds: ρ_{HV} minimum, Z_H
309 maximum, and N_{BB} in a prescribed radar sector. The allowable range of ρ_{HV} values is similar to
310 Giangrande et al. (2008, 0.90 to 0.97) but we found that using a lower threshold of 0.91 instead
311 of 0.90 slightly reduced detection of predominantly convective periods. Similar to Gourley and
312 Calvert (2003), there was little sensitivity to the minimum bright band Z_H exceedance value.
313 Most radar scan cycles were also relatively insensitive to N_{BB} as stratiform echo was often
314 widespread, encompassing a significant portion of the radar sector. The periods of largest
315 sensitivity to N_{BB} were often associated with a transition phase such as a frontal passage.
316 Through visual confirmation with individual RHI scans, a threshold of N_{BB} exceeding 35% of

Accepted for publication in *Journal of the Atmospheric Sciences*. DOI 10.1175/JAS-D-21-0091.1.

317 the radar sector's grid points was determined to effectively discriminate between a spatially
318 homogeneous bright band and convective or transient features.
319 Radar-derived bright band heights were evaluated against the 0°C height from soundings
320 launched at the NPOL site and from the NARR dataset within one hour of the radar scan cycle.
321 During the first IOP, radar-derived bright band heights averaged 138 m below the sounding-
322 derived 0°C isotherm with a root mean squared error (RMSE) of 284 m and 198 m below the
323 NARR 0°C isotherm with a RMSE of 310 m. This performance is similar to that of the algorithm
324 used by White et al. (2002) which produced radar-derived bright band heights in coastal
325 California, on average, 192 m below the sounding-derived 0°C isotherm.
326
327 *b. Secondary Z_H Maximum Detection*
328 We consider a secondary Z_H maximum to be a layer above the bright band where at the lower
329 extent, Z_H increases with height and at the upper extent, Z_H returns to decreasing with height
330 (Fig. 2a). Thus, secondary Z_H maximum detection uses only Z_H as an input, intentionally
331 removing the possibility of prescribing any polarimetric or Doppler radar signature. The
332 algorithm searches for a secondary Z_H maximum in any radar scan cycle having a bright band as
333 well as in the scan cycle immediately (~20 minutes) before and after. The search procedure is
334 performed as follows:
335 1. At each horizontal grid point within a radar sector, beginning at 1 km above the bright
336 band and searching upwards, the algorithm searches for an increase in Z_H with height
337 from the level immediately below. The increase must occur over a minimum of two 250-
338 m vertical levels. The initial level of increase in Z_H with height establishes the lower
339 extent of the secondary Z_H maximum, SM_{lwr}. The upper extent of the secondary Z_H

Accepted for publication in *Journal of the Atmospheric Sciences*. DOI 10.1175/JAS-D-21-0091.1.

maximum, SM_{upr}, is the highest vertical level with a Z_H value exceeding that at the level immediately below SM_{lwr}. Grid-point secondary Z_H maxima must have at least one vertical level that exceeds 17 dBZ.

2. Within the sector, the most frequently occurring level of the SM_{lwr} layer is identified. This level is then used to identify a horizontal layer in which a secondary Z_H maximum commonly occurs over the sector by disregarding grid points with a SM_{lwr} layer beyond 750 m above or below this level.
3. If the remaining number of grid points that have a secondary Z_H maximum, N_{SM}, exceeds 20% of the radar sector total, a secondary Z_H maximum is identified for that radar scan cycle and heights of individual grid-point SM_{lwr} and SM_{upr} layers are independently averaged to produce a secondary Z_H maximum layer.
4. In the event that an additional Z_H maximum is identified above the secondary Z_H maxima by the same criteria as the first, a decision is made about where the layer of interest exists. If the two layers are separated by less than 500 m, both layers are used and are considered as one larger layer. If, however, there are two distinct layers, the layer at a height nearest to that of the secondary Z_H maximum in the previous radar scan cycle is used.

The bright band existence precondition in the secondary Z_H maximum search was appropriate for the OLYMPEX dataset for which 0°C heights were always above ground level at the radar. However, without first being modified, this approach would not be suitable in places such as the intermountain west where freezing temperatures at the ground are expected. Nonetheless, spatial variability in the height of the bright band is not uncommon, especially in

Accepted for publication in *Journal of the Atmospheric Sciences*. DOI 10.1175/JAS-D-21-0091.1.

complex terrain. Initializing the upward search at 1 km above the average bright band height restricts detection to the cloud's ice layer, above any bright band variability.

Similar to the use of a minimum Z_H threshold for bright band detection, a grid-point minimum Z_H threshold for a secondary Z_H maximum was used to avoid detecting slight increases that can occur near echo tops. This threshold was determined by compositing average Z_H vertical profiles from all NPOL scan cycles after first being vertically adjusted to a bright band relative sense by placing the zero-height reference at the bright band. Beginning at echo top and moving down in the composite vertical Z_H profiles above the bright band from each radar sector, the rate of increase of Z_H with decreasing height aloft has a relative maximum approximately at or below 17 dBZ (Fig. 2b). In the averaged profiles, values greater than 17 dBZ contribute to the increased rate of change in Z_H aloft. The threshold of N_{SM} exceeding 20% of the total grid points in a radar sector to define a secondary Z_H maximum was arrived at in a similar manner as in the bright band detection. Visual comparison of individual RHI scans provided the basis for determining this threshold and, therefore, it is specific to the OLYMPEX dataset and the S-band NPOL radar. As discussed in two case studies in section 4b, secondary Z_H maxima tend to be less widespread than the bright band, thus a threshold below 35% is necessary, but if a value much less than 20% was used, undesirable isolated or convective features were also identified.

4. Results

The OLYMPEX field campaign successfully measured multiple midlatitude cyclones that produced widespread and orographically enhanced precipitation over the Olympic Mountains. Secondary Z_H maxima were frequently identified in the stratiform radar echo of those storms. Figure 3a, b is an example of the reflectivity field from NPOL RHIs during the 03 December

Accepted for publication in *Journal of the Atmospheric Sciences*. DOI 10.1175/JAS-D-21-0091.1.

2015 stratiform rain event in a cross-sectional view from southwest to northeast. At this time, the mean bright band height was about 2 km above NPOL. Above the bright band, a secondary Z_H maximum layer occurred over the terrain between about 4 and 4.5 km and is most pronounced beyond about 35 km from NPOL (dashed black ellipse on Fig. 3b). Over the upstream ocean, a sufficiently widespread secondary Z_H maximum meeting our detection criteria was not identified at this time. Using all NPOL radar scans, we assess how the secondary Z_H maximum manifests over the terrain relative to upstream.

a. Statistical Characteristics of the Secondary Z_H Maximum

Of all NPOL scan cycles, a bright band was identified in 20% to 23% of scan cycles over each of the four upstream oceanic radar sectors and in 41% of terrain-focused radar sector scan cycles. The median bright band height over all four ocean sectors was approximately 1.7 km above NPOL (Fig. 4a). Over the terrain, the median height decreased to 1.4 km, a common property of stratiform precipitation on windward slopes (e.g., Marwitz 1983, 1987; Medina et al. 2005; Minder et al. 2011). Bright band heights over the terrain were statistically significantly different from each of the four oceanic sectors based on a two-tailed t-test at a 95% significance level.

During periods with a bright band, a secondary Z_H maximum was identified in 10% to 11% of the radar scan cycles over each of the four oceanic radar sectors and in 25% of the terrain-focused radar sector scan cycles. The higher frequency of occurrence over the terrain was most pronounced at larger radial distances. About 25% of the terrain-focused radar scan cycles had a secondary Z_H maximum between 40 to 60 km compared to about 20% in the coastal lowland region between 10 and 30 km. Analysis of NARR data within one hour of radar scans (not

Accepted for publication in *Journal of the Atmospheric Sciences*. DOI10.1175/JAS-D-21-0091.1.

409 shown) indicated that secondary Z_H maxima were observed in diverse synoptic conditions.
410 However, they were most frequently observed in southeasterly to southwesterly low-level flow
411 having moist neutral stability and IVT greater than about 250 kg m^{-1} s^{-1}, conditions common to
412 the warm sector of midlatitude cyclones and to atmospheric river events. The structure of the
413 secondary Z_H maximum varies by storm but is approximately a 750-m-deep layer between 1.5
414 km and 3 km above the bright band with temperatures between about -6°C and -12°C (Fig. 4b,
415 c), and occasionally colder over the terrain due to apparent lifting of the secondary Z_H maximum
416 layer as flow encounters the terrain. Column-averaged Z_H within individual grid point secondary
417 Z_H maximum layers were used as a measure of the layer's intensity. Relative to the upstream
418 ocean, higher average Z_H values over the terrain (Fig. 4d) suggest an orographic enhancement of
419 the secondary Z_H maximum layer. McMurdie et al. (2018) presented similar findings of a
420 pronounced increase in frequency of large Z_H values aloft over terrain when compared to over
421 the ocean, particularly during warm sector conditions. However, by explicitly identifying the
422 secondary Z_H maxima feature, we have demonstrated that it can form upstream. This finding
423 suggests that the physical processes that result in a secondary Z_H maximum are not necessarily
424 unique to orographically modified flow but are enhanced by flow over the windward slopes. The
425 following section uses dual-polarization radar and in situ measurements to identify the
426 microphysical processes that produce the relatively high Z_H in the secondary Z_H maximum layer
427 over the windward slopes.
428
429 *b. Microphysics Case Studies*
430 The Citation aircraft was deployed within the range of NPOL a total of 20 times during
431 OLYMPEX. The secondary Z_H maximum layer was directly sampled by the Citation on six

Accepted for publication in *Journal of the Atmospheric Sciences*. DOI 10.1175/JAS-D-21-0091.1.

flights, four of which provided in situ observations within a deep portion of the cloud's ice layer. Analysis is presented below for two diverse storms that both featured a persistent secondary Z_H maximum in a similar location over the windward slopes for the duration of the flight. The 03 December flight occurred during the warm sector portion of the midlatitude cyclone having synoptic conditions most similar to those commonly observed during secondary Z_H maxima events. The flight during the preceding cyclone on 01-02 December occurred during the prefrontal portion; conditions that were less frequently associated with secondary Z_H maxima events. The synoptically different conditions between the warm-sector and prefrontal periods of these two events make for a unique comparison of in situ measurements and inferred dynamic processes associated with secondary Z_H maxima development.

1. CASE STUDY: 03 DECEMBER 2015

The 03 December storm featured significant orographic enhancement resulting in 100 to 200 mm of rain at high elevations on the windward slopes of the Olympic Mountains (Petersen et al. 2017b). The NPOL sounding at 1516 UTC (Fig. 5) shows southerly flow at 925 hPa, south-southwesterly at 700 hPa, near-neutral moist static stability in the 950-850 hPa layer, and IVT of 784 kg m^{-1} s^{-1} (Zagrodnik et al. 2019). Over the terrain, a secondary Z_H maximum was continuously identified from 1252 UTC to 1652 UTC. During this time, the Citation flew in a series of vertically stacked legs of constant elevation oriented approximately northwest to southeast over the windward slopes (Fig. 6). In situ observations were organized in three distinct vertical layers as illustrated schematically in Fig. 7a. In radar scan cycles coinciding with in situ observations, the SM_{lwr} and SM_{upr} levels respectively ranged from 1.62 to 2 km and 2.27 to 2.62 km above the bright band. To distinguish between layers, a 250-m separation is used between

Accepted for publication in *Journal of the Atmospheric Sciences*. DOI 10.1175/JAS-D-21-0091.1.

455 SM_{lwr} and the layer below and between SM_{upr} and the layer above. The flight resulted in 445,
456 541, and 528 1 Hz in situ observations from above, within, and below the secondary Z_H
457 maximum, respectively, largely within a radial range of 40 to 60 km from NPOL. Temperatures
458 for the top and bottom of each layer obtained from the 1516 UTC sounding indicate that the 1-
459 km layer below terminates just above the bright band at -2.0°C. The layer above (orange shading,
460 Fig. 7a) nearly resembles a temperature range that is commonly associated with dendritic ice
461 growth (Bailey and Hallett 2009).

462 At S band, radar scattering is generally in the Rayleigh regime and attenuation effects are
463 small such that radar reflectivity is proportional to the sixth power of particle's mass-equivalent
464 diameter and, therefore, dominated by the contributions of large particles. Thus, we evaluate how
465 the distribution of particle sizes changes through the ice layer of the cloud. Figure 7b shows the
466 frequency of time that particles of a given size were observed by the 2D-S and HVPS-3 OAPs.
467 The most striking differences between the three layers are at sizes greater than about 2 mm.
468 Above the secondary Z_H maximum, particles greater than 2 mm were rarely observed but within
469 and below the secondary Z_H maximum, large particles were frequently observed up to about 10
470 mm in size. The flight-averaged spectral IWC (Fig. 7c) peaks in the secondary Z_H maximum
471 layer relative to the layers above and below between about 2 to 10 mm, an indication of rapid
472 hydrometeor growth within this layer. Below the secondary Z_H maximum, spectral IWC
473 decreases in the 2 to 10 mm size range but increases for small particle sizes below about 1 mm.
474 The cumulative reflectivity, Z_{PSD}, increases rapidly with diameter for particles greater than about
475 2 mm, underscoring the sixth-power dependence on particle diameter (Fig. 7d).

476 Of the nine possible UIOOPS habit classes, the relatively high spectral IWC for 2 to 10
477 mm-sized particles in the secondary Z_H maximum layer was dominated by dendritic and irregular

Accepted for publication in *Journal of the Atmospheric Sciences*. DOI 10.1175/JAS-D-21-0091.1.

habits (Fig. 7e, f). Figure 8 includes imagery of select particles that are broadly representative of the full set of images collected by the 2.3 μm-resolution Cloud Particle Imager (CPI) above, within, and below the secondary Z_H maximum layer. The prevalence of dendritic and irregular habit types from UIOOPS is consistent with observations from the CPI (Fig. 8a, b).

To put the in situ measurements in a context of radar-based inferences of ice microphysics, averaged vertical profiles of Z_H and Z_{DR} were constructed. Vertical columns of NPOL data at grid points containing a secondary Z_H maximum were averaged over the radar sector and then adjusted to a bright band relative framework. Figure 9 shows the averaged vertical profiles coinciding with the 1432 to 1552 UTC portion of the Citation flight and the average positions of the secondary Z_H maximum layer and the layers above and below, shaded by color according to the schematic in Fig. 7a. There is a local maximum in Z_{DR} between 3 and 3.5 km above the bright band indicating the presence of horizontally oriented ice particles (Fig. 9b). The maximum in Z_{DR} occurs near an onset of rapid increase in Z_H with decreasing height (within the layer above the secondary Z_H maximum, shaded in orange in Fig. 9a). Although the secondary Z_H maximum maintains an approximately steady state during the Citation flight, there is some inherent variability of the secondary Z_H maximum in both vertical position and magnitude. As a result, averaging over the radar domain results in a smoothed Z_H profile with minimal apparent maximum aloft. However, there is a distinct change in the slope of the Z_H profile as a result of the Z_H maximum between 2 and 2.5 km above the bright band in each scan cycle (top of secondary Z_H maximum layer, shaded in violet in Fig. 9a). In the latest two scan cycles (1612 and 1632 UTC), the Z_{DR} maximum layer aloft apparently repositions itself below the secondary Z_H maximum layer to approximately 1 to 1.5 km above the bright band. This time period coincides with a breakup of the upstream stratiform precipitation. While the cause of the

Accepted for publication in *Journal of the Atmospheric Sciences*. DOI 10.1175/JAS-D-21-0091.1.

apparent repositioning of the Z_{DR} maximum layer is unclear, the secondary Z_H maximum persists through the 1652 UTC radar scan cycle.

Above the secondary Z_H maximum near the local maximum in Z_{DR} (i.e., 3 to 3.5 km above the bright band where temperatures near -15°C; orange shading, Fig. 9b), in situ observations of nearly pristine or lightly aggregated branched and planar crystals (Fig. 8a) suggest that vapor deposition is the primary ice growth process. Below the local maximum in Z_{DR}, there is a sharp downward increase in Z_H and decrease in Z_{DR} (orange shading, Fig. 9a, b) and heavily rimed crystals and aggregates were observed in the secondary Z_H maximum layer (Fig. 8b). Supercooled liquid water, measured by the King probe, averaged 0.1 g m^{-3} in both the secondary Z_H maximum layer and the layer above (Fig. 7a). These polarimetric signatures could be explained by aggregation alone (Kennedy and Rutledge 2011); however, riming of plate-like crystals has a similar polarimetric signature (Schrom and Kumjian 2016). Indeed, the particle imagery indicates that aggregation and riming processes were occurring concurrently (Fig. 8b).

Depositional ice growth requires ice supersaturation and dendritic growth typically occurs when ice supersaturation is near water saturation (Bailey and Hallett 2009). Maintenance of supercooled liquid water necessary for riming also requires high ice supersaturation. Thus, conditions favorable for dendritic growth also favor riming. Previous studies have suggested that supercooled liquid water transport can be effective within turbulent overturning cells that additionally enhance aggregation efficiency by increasing the probability of particle collision (Houze and Medina 2005; Medina et al. 2007). In the radial velocity field of the 1453 UTC RHI, there is evidence of a low-level jet over the upstream ocean that is forced aloft as it encounters the windward slopes (Fig. 3e, f). The secondary Z_H maximum occurs over the windward slopes near a sheared layer at the top of the low-level jet and immediately below a layer of enhanced

Accepted for publication in *Journal of the Atmospheric Sciences*. DOI 10.1175/JAS-D-21-0091.1.

spectrum width, indicative of turbulent air motion (Fig. 3h). This pattern was consistent across other terrain-focused RHIs during the 03 December event. The forced ascent of the low-level jet facilitates the advection of liquid water above the bright band whereby rimed mass is accumulated most efficiently by larger particles (e.g., Johnson 1987). The turbulent region above the secondary Z_H maximum is expected to increase particle collisions, enhancing aggregation and therefore, the rate of rimed mass growth.

2. CASE STUDY: 01-02 DECEMBER 2015

In the passage of a weakening upper-level trough from approximately 2000 UTC 01 December to 0600 UTC 02 December, windward slopes of the Olympic Mountains received approximately 30 to 50 mm of stratiform precipitation (Petersen et al. 2017b). The Citation sampled the prefrontal portion of the storm in a vertical spiral over the windward slopes between 3 and 7 km MSL where temperatures were about -5°C to -30°C (Fig. 10). The winds in the 2317 UTC 01 December sounding were overall weaker than on 03 December and included a slightly more easterly component at the surface (Fig. 5). The IVT was also less than for the 03 December event albeit relatively high at 500 kg m^{-1} s^{-1} (Zagrodnik et al. 2019). However, the most notable difference between these two events was the low-level stability. The 01-02 December event was moist stable in the 950 to 850 hPa layer (N_m^2 = 1.06 x 10^{-4} s^{-2}) whereas the 03 December was moist neutral (N_m^2 = -0.21 x 10^{-4} s^{-2}, Zagrodnik et al. 2019).

During the 01-02 December event, a secondary Z_H maximum was rarely identified over the upstream ocean but was consistently identified over the windward slopes between 2132 UTC 01 December and 0552 UTC 02 December, with the exception of the 0032 UTC and 0132 UTC scan cycles on 02 December. Secondary Z_H maxima were most pronounced beyond 30 km from

Accepted for publication in *Journal of the Atmospheric Sciences*. DOI 10.1175/JAS-D-21-0091.1.

NPOL (dashed black ellipse on Fig. 11b) between the Prairie Creek and Wynoochee ground sites and where the primary ascending and descending Citation spiral occurred (Fig. 10). During the flight, 112, 98, and 487 1 Hz in situ observations were collected from above, within, and below the secondary Z_H maximum, respectively. The SM_{lwr} and SM_{upr} levels coinciding with in situ observations respectively ranged from 1.56 to 1.7 km and 2.05 to 2.24 km above the bright band. The secondary Z_H maximum layer spanned -7.0°C to -9.9°C (Fig. 12a) at the time of the 2317 UTC sounding. Supercooled liquid water was observed in the secondary Z_H maximum layer with an average value of 0.11 g m^{-3}.

As on 03 December, large ice particles (> 2 mm) were observed much more frequently and with a higher flight-averaged spectral IWC within the secondary Z_H maximum layer relative to the layers above and below (Fig. 12b, c). At 1 mm, disagreement between the 2D-S and HVPS-3 probe measurements appears significant. Sizing errors increase as particle size becomes small relative to the OAP resolution due to fewer pixels available to resolve the particle (Korolev et al. 1998). Thus, we expect measurements from HVPS-3 near the 1-mm transition size to have the greatest uncertainties. However, spectral IWC at this size range does not significantly affect the computed radar reflectivity estimates (Fig. 12d). Calculated cumulative Z_{PSD} is similar in all three layers up to approximately 2 mm, but at larger sizes, Z_{PSD} is enhanced in the secondary Z_H maximum layer as a result of increases in spectral IWC dominated by dendritic and irregular habit classes (Fig. 12e, f).

Despite synoptic differences between the 03 December and 01-02 December events, average PSDs from each flight suggest that similar increases in spectral IWC at large particle sizes resulted in the increased Z_H within the secondary Z_H maximum layer. Correspondingly, the average vertical Z_H profiles for each event are similar, although on 01-02 December, the

Accepted for publication in *Journal of the Atmospheric Sciences*. DOI 10.1175/JAS-D-21-0091.1.

secondary Z_H maximum occurs about 1.75 to 2.25 km above the bright band (violet shading, Fig. 13a), slightly lower than on 03 December. A maximum in Z_{DR} occurs near cloud top and decreases steadily to a minimum just above the bright band. Although these profiles lack a distinct signature of a dendritic growth zone in the form of a Z_{DR} maximum, individual rimed and unrimed plate-like crystals were observed above the secondary Z_H maximum (Fig. 14a) where the average Z_{DR} exceeds 0.4 dB, which is expected for a mixed population of dendritic crystals with varied degrees of riming and aggregation. Immediately above the secondary Z_H maximum layer, from about 2.5 to 3 km above the bright band, the rapid downward increase in Z_H and continued decrease in Z_{DR} (orange shading, Fig. 13b) are consistent with onset of aggregation and possibly riming. The two events had similar LWC values in the secondary Z_H maximum layer (~0.1 g m^{-3}) but the LWC that was observed above the secondary Z_H maximum layer on 03 December averaged 0.1 g m^{-3}, whereas in the 01-02 December event, no supercooled liquid water was observed. Because riming efficiency increases with LWC (Jensen and Harrington 2015), it is probable that mass growth by riming above the secondary Z_H maximum was less efficient on 01-02 December than during the 03 December event. This inference appears to be supported by in situ particle observations from the CPI probe which generally show a lesser degree of riming for the 01-02 December event, especially above the secondary Z_H maximum (Fig. 14a). Within the secondary Z_H maximum layer, however, riming was apparent in much of the particle imagery (Fig. 14b).

Previous studies have shown strong updrafts to be an effective indicator of riming processes (Moisseev et al. 2009; Schrom and Kumjian 2016). Based on heavier riming observed in the secondary Z_H maximum layer and overall higher LWC aloft on 03 December, it is plausible that the updraft region over the windward slopes was either more intense or more

Accepted for publication in *Journal of the Atmospheric Sciences*. DOI 10.1175/JAS-D-21-0091.1.

vertically extensive than during the 01-02 December event. In the radial velocity field of the 2313 UTC 01 December RHI over the windward slopes, blocked low-level southeasterly terrain-parallel flow is evident by the negative radial velocity indicating flow towards the radar (Fig. 11f). Ascent can be inferred in the lifting of the low-level jet, but the stable layer acts as an upstream barrier extension effectively reducing the slope of the mountain. The mean flow is also notably weaker than on 03 December; thus, the inferred updraft over the windward slopes is also weaker. However, much like the 03 December event, the secondary Z_H maximum region coincides with a sheared layer in the radial velocity field immediately below a layer of enhanced spectrum width over the windward slopes beyond 30 km (Fig. 11f, h). Even with higher low-level static stability than the 03 December event, liquid water was apparently transported aloft by orographically-forced ascent of a low-level jet. The in situ observations and inferred microphysical processes associated with the secondary Z_H maxima of the 01-02 December event are similar to those of the 03 December event. Above the secondary Z_H maximum, branched and planar crystals readily aggregated, likely enhanced by turbulent air motion, and subsequently accumulated rimed mass to produce high spectral IWC at large particle sizes. In the following section, these microphysical properties are evaluated within the broader OLYMPEX dataset to assess general properties of the secondary Z_H maxima layer.

c. *Comparison of Secondary Z_H Maximum and Bright-Band-Only Periods*

To distinguish properties unique to secondary Z_H maxima, we compare observations from all OLYMPEX secondary Z_H maxima periods to bright-band-only periods (i.e., radar scan cycles with a bright band but no secondary Z_H maximum). In situ observations during bright-band-only periods were compared to secondary Z_H maximum periods by using temperature layers similar to

Accepted for publication in *Journal of the Atmospheric Sciences*. DOI 10.1175/JAS-D-21-0091.1.

616 those of the two case studies. Temperatures of -6°C to -12°C represent the layer that a secondary
617 Z_H maximum would be likely to form, -12°C to -18°C, the layer above and 0°C to -6°C, the layer
618 below as illustrated in Fig. 15a. During bright-band-only periods from all flights, measurements
619 within each layer were used to calculate average PSDs separately for the upstream ocean and the
620 windward terrain (Fig. 15b, c). Observations collected in the 0°C to -6°C layer on the 18
621 December flight were removed due to sampling at the bright band. Unfortunately, no
622 observations were made within a secondary Z_H maximum layer over the upstream ocean.

623 Unlike during the 01-02 and 03 December secondary Z_H maximum periods, there is no
624 apparent increase in the average IWC for the -6°C to -12°C layer relative to the layers above and
625 below over the ocean or over terrain. Averaging over several flights in this manner is subject to a
626 sampling bias depending on which layers were sampled for any given storm. However, each
627 layer's average PSD is constructed from a minimum of two separate flights. The average spectral
628 IWC is substantially higher at larger sizes in the secondary Z_H maximum periods when compared
629 to any other temperature layer during bright-band-only periods (Fig. 15c). Ice-phase growth
630 regimes specified by temperature alone cannot sufficiently describe the observed differences in
631 the vertical profile of Z_H between secondary Z_H maximum and bright-band-only periods.

632 Riming in the secondary Z_H maximum layer for both case studies motivates exploring
633 LWC measurements for all secondary Z_H maximum and bright-band-only periods.
634 Measurements of LWC exceeding 0.05 g m^{-3} from the King probe in each bright-band-only
635 vertical layer are shown in Fig. 16. The most frequent observations of supercooled liquid water
636 over the ocean are found just above the bright band in the 0°C to -6°C layer and rarely in the
637 colder layers. Indeed, the RICE instrument indicated icing conditions in 24% of observations in
638 the 0°C to -6°C layer and in zero observations in either layer above. Over the terrain, the RICE

Accepted for publication in *Journal of the Atmospheric Sciences*. DOI 10.1175/JAS-D-21-0091.1.

instrument indicated icing in 13% of the observations in the bright-band-only -6°C to -12°C layer but 24% in the secondary Z_H maximum layer. In general, supercooled liquid water was found more frequently over the terrain when compared to over the upstream ocean in all layers, but especially during secondary Z_H maximum periods. The prevalence of riming due to supercooled liquid water in the secondary Z_H maximum layer over the windward slopes has implications for the density, and thus fall velocity, of ice-phase particles (e.g., Jensen and Harrington 2015). We hypothesize that the rate of rimed mass growth for some secondary Z_H maxima layer particles can be sufficient to overcome windward updraft velocities before being transported to the lee slopes, enhancing windward precipitation. Fallout of relatively large ice-phase hydrometeors implies a larger mass flux through the melting level, thus an increase in bright band Z_H values and possibly surface accumulations.

Over the terrain-focused radar sector, histograms of bright-band Z_H values at individual grid points during all secondary Z_H maxima and bright-band-only periods are compared in Fig. 17. During bright-band-only periods, Z_H was most frequently between 25 and 30 dBZ but during secondary Z_H maximum periods, there is a distinct shift in the peak of the distribution to about 35 to 40 dBZ with a marginal increase in the mean value. Below the bright band, at the surface, precipitation characteristics were evaluated at three windward sites during secondary Z_H maxima and bright-band-only periods (Fig. 18). Because of the uncertainties in ice particle trajectories over Pacific Northwest coastal mountains (Hobbs et al. 1973; Colle and Zeng 2004; Colle et al. 2005), we do not attempt to relate the location or magnitude of the secondary Z_H maximum layer to the ground sites. Rather, we evaluate how the observed precipitation characteristics within the terrain-focused sector differ when a secondary Z_H maximum was present and when only a bright band was present.

Accepted for publication in *Journal of the Atmospheric Sciences*. DOI 10.1175/JAS-D-21-0091.1.

During secondary Z_H maximum periods, rain rate increased, and mass-weighted mean drop diameter was larger at all three ground sites relative to bright-band-only periods with the most significant increases at the mid-mountain site, Prairie Creek (Fig. 18). The greater increases at Prairie Creek compared to Fishery are likely attributable to the preferential formation of secondary Z_H maxima over mid- to high-elevation terrain. At the higher elevation Wynoochee site, the depth of the warm-rain layer is shallower than at Prairie Creek, thus the overall contribution of warm-rain processes that produce smaller drops (Zagrodnik et al. 2018) is already reduced. Therefore, the effect of additional melted ice particles during secondary Z_H maximum periods is apparently less pronounced than at lower sites. The surface observations are consistent with our hypothesis of windward fallout of large, heavily rimed particles from the secondary Z_H maximum layer. However, this analysis does not preclude contributions from concurrent embedded convective cells or enhanced warm-rain processes. Thus, the extent to which the secondary Z_H maximum layer is the cause of increased rain rates and drop diameters on windward slopes is uncertain. This interesting finding warrants further investigation in future numerical modeling studies to determine possible trajectories of secondary Z_H maxima layer particles, elucidating the effect of precipitation formed in this layer by connecting it to the surface.

5. Discussion and Conclusions

During winter storms over North American western coastal mountains, previous studies have documented a secondary Z_H maximum layer above the radar bright band (Houze and Medina 2005; Kingsmill et al. 2006; Medina et al. 2007; McMurdie et al. 2018). These previous studies raised several questions about the role of topography on the development of the

Accepted for publication in *Journal of the Atmospheric Sciences*. DOI10.1175/JAS-D-21-0091.1.

secondary Z_H maximum layer, the microphysical properties associated with this layer, and its effect on windward precipitation. We have used observations over the upstream ocean and over the windward slopes of the Olympic Mountains during OLYMPEX to investigate the microphysical properties of ice particles within secondary Z_H maximum layers and discern the influence of orography. This study has resulted in the following conclusions:

- Secondary Z_H maxima layers are observed upstream but its frequency of occurrence and layer-average Z_H are enhanced over the windward slopes, indicating an orographic enhancement of ice-phase precipitation processes.
- Relatively high Z_H values of the secondary Z_H maximum layer are a result of high concentrations of large (~2 to 10 mm diameter) hydrometeors typically formed of aggregated dendritic or irregular branched crystals that are often heavily rimed.
- Analysis of two case studies shows that when a secondary Z_H maxima layer is observed over the windward slopes, it commonly occurs near high velocity shear at the top of a cross-barrier low-level jet and below a turbulent layer indicated by a local maximum in spectrum width.
- The presence of a secondary Z_H maxima layer is associated with increased rain rates and larger mass-weighted mean drop diameters at windward ground sites.

Investigations of the microphysics of ice-phase precipitation processes have often been limited to inferences of those processes based largely on polarimetric radar signatures (e.g., Kennedy and Rutledge 2011; Schrom et al. 2015; Kumjian and Lombardo 2017). Enhanced Z_{DR} near -15°C temperatures often indicates a dendritic growth zone and is consistent with in situ particle imagery for the two case studies presented in section 4b. The regularity in formation of

Accepted for publication in *Journal of the Atmospheric Sciences*. DOI10.1175/JAS-D-21-0091.1.

the secondary Z_H maximum at temperatures just warmer than the dendritic growth zone (-6°C to -12°C) and just below enhanced Z_{DR} indicates that a secondary Z_H maximum is not so much a signature of dendrites being present as much as an increase in the size of particles due to aggregation. Similar to Houze and Medina (2005), we speculate that aggregation is enhanced within shear-induced turbulent overturning cells during stably stratified and moist-neutrally stable low-level conditions. As aggregation is enhanced, individual particle sizes are increased, thus favoring more efficient accumulation of rimed mass which increases particle fall velocity, and therefore, the rate of fallout on the windward slopes. Orographic lifting of a low-level jet appears to efficiently maintain supercooled liquid water aloft for riming.

The relative impacts of ice-phase and warm-rain processes in orographically-enhanced windward precipitation over the Olympic Mountains is a topic that has received significant discussion in recent studies (e.g., Zagrodnik et al. 2018; Conrick and Mass 2019a, 2019b; Zagrodnik et al. 2021). These studies have demonstrated that warm-rain processes significantly contribute to the observed windward precipitation enhancement. Our findings suggest that ice particles formed in secondary Z_H maxima layers may additionally enhance windward precipitation. Larger mean drop diameters observed at all three ground sites during secondary Z_H maximum periods are an indication of accelerated ice growth aloft that facilitated the fallout of large particles to increase rain rates on the windward slopes.

Within the range of NPOL over the windward slopes, composites of high-resolution numerical modeling simulations by Zagrodnik et al. (2021) indicated that vertical velocities in the ice layer averaged approximately 0.2 to 1 m s^{-1} during prefrontal (01-02 December) and warm-sector (03 December) periods. We hypothesize that ice particles unable to grow fast enough to achieve a mass necessary for windward fallout are advected downstream in the low-

Accepted for publication in *Journal of the Atmospheric Sciences*. DOI 10.1175/JAS-D-21-0091.1.

level cross-barrier flow. Indeed, such differential advection may explain the slight decrease in Z_H below the secondary Z_H maximum layer. Alternatively, reduced Z_H values below the secondary Z_H maximum layer may be a result of decreased particle sizes due to breakup. Fragmented ice crystals (i.e., dendrite arms) were occasionally observed in the particle imagery (not shown), an indication of mechanical ice-ice collision fragmentation. Additionally, needles were observed in the particle imagery (Fig. 8c), suggesting that rime-splintering (Hallet and Mossop 1974) was likely occurring. Such riming may have also resulted in particle fragmentation from thermal shock (Korolev and Leisner 2020).

Results from this study emphasize riming as a mass growth process complementary to aggregation in the secondary Z_H maximum layer that has implications for particle densities. The rate of rimed mass growth increases with particle size (Johnson 1987) and, indeed, flight-averaged PSDs from both case studies in section 4b showed a size dependency in which significant spectral IWC was present at large particle sizes (> ~2 mm diameter) within the secondary Z_H maximum layer. These results have likely implications for remote sensing retrievals of precipitation over complex terrain. In general, remote sensing retrievals require assumptions about the snow density and shape of the PSD, properties that undergo distinct modification within the secondary Z_H maximum layer. Future work will investigate the suitability of these retrieval assumptions and their effect on precipitation rate estimates over complex terrain using coincident in situ and airborne remote sensing retrievals.

Acknowledgments.

The authors thank the Quinault Indian Nation and the staff of the Olympic National Park and U.S. Forest Service for permission to install and operate instrumentation on their land. The

Accepted for publication in *Journal of the Atmospheric Sciences*. DOI 10.1175/JAS-D-21-0091.1.

authors also thank the entire OLYMPEX team for successful data collection during the campaign. Dr. Joseph Finlon assisted with the UIOOPS processing and interpretation of the microphysics probe data. Dr. Joseph Boomgard-Zagrodnik provided code for processing the disdrometer data and assisted in its interpretation. Beth Tully provided graphics support for Figures 8 and 14. The authors also thank Profs. Roger Marchand and Dale Durran for their useful discussions and feedback on this work. Comments from three anonymous reviewers significantly improved this manuscript. This research was supported by NSF grant AGS-1657251.

Data Availability Statement.

All data from OLYMPEX used in this study are available from the NASA Distributed Active Archive Center at https://ghrc.nsstc.nasa.gov/uso/ds_details/collections/gpmolyxC.html (Petersen et al. 2018). NCEP Reanalysis data was provided by NOAA/OAR/ESRL PSL, Boulder, Colorado, USA, from their web site at https://psl.noaa.gov/data/gridded/data.narr.html.

Accepted for publication in *Journal of the Atmospheric Sciences*. DOI 10.1175/JAS-D-21-0091.1.

REFERENCES

Andrić, J., M. R. Kumjian, D. S. Zrnić, J. M. Straka, and V. M. Melnikov, 2013: Polarimetric Signatures above the Melting Layer in Winter Storms: An Observational and Modeling Study. *J. Appl. Meteor. Climatol.*, **52**, 682–700, https://doi.org/10.1175/JAMC-D-12-028.1.

Bailey, M. P., and J. Hallett, 2009: A Comprehensive Habit Diagram for Atmospheric Ice Crystals: Confirmation from the Laboratory, AIRS II, and Other Field Studies. *J. Atmos. Sci.*, **66**, 2888–2899, https://doi.org/10.1175/2009JAS2883.1.

Baker, B., and R. P. Lawson, 2006: Improvement in Determination of Ice Water Content from Two-Dimensional Particle Imagery. Part I: Image-to-Mass Relationships. *J. Appl. Meteor. Climatol.*, **45**, 1282–1290, https://doi.org/10.1175/JAM2398.1.

Bechini, R., L. Baldini, and V. Chandrasekar, 2013: Polarimetric Radar Observations in the Ice Region of Precipitating Clouds at C-Band and X-Band Radar Frequencies. *J. Appl. Meteor. Climatol.*, **52**, 1147–1169, https://doi.org/10.1175/JAMC-D-12-055.1.

Bell, M. M., M. Dixon, B. Javornik, W.-C. Lee, B. Melli, J. DeHart and T.-Y. Cha, 2020: nsf-lrose/lrose-cyclone: lrose-cyclone-20200110, https://doi.org/10.5281/zenodo.3604387.

Brandes, E. A., and K. Ikeda, 2004: Freezing-Level Estimation with Polarimetric Radar. *J. Appl. Meteor.*, **43**, 1541–1553, https://doi.org/10.1175/JAM2155.1.

Brdar, S., and A. Seifert, 2018: McSnow: A Monte-Carlo Particle Model for Riming and Aggregation of Ice Particles in a Multidimensional Microphysical Phase Space. *J. Adv. Model. Earth Syst.*, **10**, 187–206, https://doi.org/10.1002/2017MS001167.

799 Brown, P. R. A., and P. N. Fancis, 1995: Improved Measurements of the Ice Water Content in
800 Cirrus Using a Total-Water Probe. *J. Atmos. Oceanic Technol.*, **12**, 410–414,
801 https://doi.org/10.1175/1520-0426(1995)012<0410:IMOTIW>2.0.CO;2.
802 Chase, R. J., and Coauthors, 2018: Evaluation of Triple-Frequency Radar Retrieval of Snowfall
803 Properties Using Coincident Airborne In Situ Observations During OLYMPEX.
804 *Geophys. Res. Lett.*, **45**, 5752–5760, https://doi.org/10.1029/2018GL077997.
805 Cober, S., A. Korolev, and G. Isaac, 2001: Assessing characteristics of the Rosemount Icing
806 Detector under natural icing conditions. *39th Aerosp. Sci. Meet. Exhib.*, Reno, NV, Amer.
807 Inst. Aeronaut. Astronaut., https://doi.org/10.2514/6.2001-397.
808 Colle, B. A., and Y. Zeng, 2004: Bulk Microphysical Sensitivities within the MM5 for
809 Orographic Precipitation. Part I: The Sierra 1986 Event. *Mon. Wea. Rev.*, **132**, 2780–
810 2801, https://doi.org/10.1175/MWR2821.1.
811 Colle, B. A., M. F. Garvert, J. B. Wolfe, C. F. Mass, and C. P. Woods, 2005: The 13–14
812 December 2001 IMPROVE-2 Event. Part III: Simulated Microphysical Budgets and
813 Sensitivity Studies. *J. Atmos. Sci.*, **62**, 3535–3558, https://doi.org/10.1175/JAS3552.1.
814 Conrick, R., and C. F. Mass, 2019a: Evaluating Simulated Microphysics during OLYMPEX
815 Using GPM Satellite Observations. *J. Atmos. Sci.*, **76**, 1093–1105,
816 https://doi.org/10.1175/JAS-D-18-0271.1.
817 Conrick, R., and C. F. Mass, 2019b: An Evaluation of Simulated Precipitation Characteristics
818 during OLYMPEX. *J. Hydrometeor.*, **20**, 1147–1164, https://doi.org/10.1175/JHM-D-18-
819 0144.1.

Accepted for publication in *Journal of the Atmospheric Sciences*. DOI 10.1175/JAS-D-21-0091.1.

820 Durran, D. R., and J. B. Klemp, 1982: On the Effects of Moisture on the Brunt-Väisälä
821 Frequency. *J. Atmos. Sci.*, **39**, 2152–2158, https://doi.org/10.1175/1520-
822 0469(1982)039<2152:OTEOMO>2.0.CO;2.
823 Giangrande, S. E., J. M. Krause, and A. V. Ryzhkov, 2008: Automatic Designation of the
824 Melting Layer with a Polarimetric Prototype of the WSR-88D Radar. *J. Appl. Meteor.*
825 *Climatol.*, **47**, 1354–1364, https://doi.org/10.1175/2007JAMC1634.1.
826 Gourley, J. J., and C. M. Calvert, 2003: Automated Detection of the Bright Band Using WSR-
827 88D Data. *Wea. Forecasting*, **18**, 585–599, https://doi.org/10.1175/1520-
828 0434(2003)018<0585:ADOTBB>2.0.CO;2.
829 Grabowski, W. W., H. Morrison, S.-I. Shima, G. C. Abade, P. Dziekan, and H. Pawlowska,
830 2019: Modeling of Cloud Microphysics: Can We Do Better? *Bull. Amer. Meteor. Soc.*,
831 **100**, 655–672, https://doi.org/10.1175/BAMS-D-18-0005.1.
832 Griffin, E. M., T. J. Schuur, and A. V. Ryzhkov, 2018: A Polarimetric Analysis of Ice
833 Microphysical Processes in Snow, Using Quasi-Vertical Profiles. *J. Appl. Meteor.*
834 *Climatol.*, **57**, 31–50, https://doi.org/10.1175/JAMC-D-17-0033.1.
835 Hallett, J., and S. C. Mossop, 1974: Production of secondary ice particles during the riming
836 process. *Nature*, **249**, 26–28, https://doi.org/10.1038/249026a0.
837 Heymsfield, A. J., A. Bansemer, C. Schmitt, C. Twohy, and M. R. Poellot, 2004: Effective Ice
838 Particle Densities Derived from Aircraft Data. *J. Atmos. Sci.*, **61**, 982–1003,
839 https://doi.org/10.1175/1520-0469(2004)061<0982:EIPDDF>2.0.CO;2.
840 Hobbs, P. V., R. C. Easter, and A. B. Fraser, 1973: A Theoretical Study of the Flow of Air and
841 Fallout of Solid Precipitation Over Mountainous Terrain: Part II. Microphysics. *J. Atmos.*

Accepted for publication in *Journal of the Atmospheric Sciences*. DOI 10.1175/JAS-D-21-0091.1.

Sci., **30**, 813–823, https://doi.org/10.1175/1520-0469(1973)030<0813:ATSOTF>2.0.CO;2.

Hogan, R. J., M. P. Mittermaier, and A. J. Illingworth, 2006: The Retrieval of Ice Water Content from Radar Reflectivity Factor and Temperature and Its Use in Evaluating a Mesoscale Model. *J. Appl. Meteor. Climatol.*, **45**, 301–317, https://doi.org/10.1175/JAM2340.1.

Holroyd, E. W., 1987: Some Techniques and Uses of 2D-C Habit Classification Software for Snow Particles. *J. Atmos. Oceanic Technol.*, **4**, 498–511, https://doi.org/10.1175/1520-0426(1987)004<0498:STAUOC>2.0.CO;2.

Houze, R. A., 2012: Orographic effects on precipitating clouds. *Rev. Geophys.*, **50**, RG1001, https://doi.org/10.1029/2011RG000365.

Houze, R. A., and S. Medina, 2005: Turbulence as a Mechanism for Orographic Precipitation Enhancement. *J. Atmos. Sci.*, **62**, 3599–3623, https://doi.org/10.1175/JAS3555.1.

Houze, R. A., and Coauthors, 2017: The Olympic Mountains Experiment (OLYMPEX). *Bull. Amer. Meteor. Soc.*, **98**, 2167–2188, https://doi.org/10.1175/BAMS-D-16-0182.1.

Jensen, A. A., and J. Y. Harrington, 2015: Modeling Ice Crystal Aspect Ratio Evolution during Riming: A Single-Particle Growth Model. *J. Atmos. Sci.*, **72**, 2569–2590, https://doi.org/10.1175/JAS-D-14-0297.1.

Johnson, D. B., 1987: On the Relative Efficiency of Coalescence and Riming. *J. Atmos. Sci.*, **44**, 1671–1680, https://doi.org/10.1175/1520-0469(1987)044<1671:OTREOC>2.0.CO;2.

Kennedy, P. C., and S. A. Rutledge, 2011: S-Band Dual-Polarization Radar Observations of Winter Storms. *J. Appl. Meteor. Climatol.*, **50**, 844–858, https://doi.org/10.1175/2010JAMC2558.1.

Accepted for publication in *Journal of the Atmospheric Sciences*. DOI 10.1175/JAS-D-21-0091.1.

King, W. D., D. A. Parkin, and R. J. Handsworth, 1978: A Hot-Wire Liquid Water Device Having Fully Calculable Response Characteristics. *Amer. Meteor. Soc.*, **17**, 1809–1813, https://doi.org/10.1175/1520-0450(1978)017<1809:AHWLWD>2.0.CO;2.

Kingsmill, D. E., P. J. Neiman, F. M. Ralph, and A. B. White, 2006: Synoptic and Topographic Variability of Northern California Precipitation Characteristics in Landfalling Winter Storms Observed during CALJET. *Mon. Wea. Rev.*, **134**, 2072–2094, https://doi.org/10.1175/MWR3166.1.

Korolev, A., and T. Leisner, 2020: Review of experimental studies of secondary ice production. *Atmos. Chem. Phys.*, **20**, 11767–11797, https://doi.org/10.5194/acp-20-11767-2020.

Korolev, A. V., J. W. Strapp, and G. A. Isaac, 1998: Evaluation of the Accuracy of PMS Optical Array Probes. *J. Atmos. Oceanic Technol.*, **15**, 708–720, https://doi.org/10.1175/1520-0426(1998)015<0708:EOTAOP>2.0.CO;2.

Kumjian, M. R., and K. A. Lombardo, 2017: Insights into the Evolving Microphysical and Kinematic Structure of Northeastern U.S. Winter Storms from Dual-Polarization Doppler Radar. *Mon. Wea. Rev.*, **145**, 1033–1061, https://doi.org/10.1175/MWR-D-15-0451.1.

Marwitz, J. D., 1983: The Kinematics of Orographic Airflow During Sierra Storms. *J. Atmos. Sci.*, **40**, 1218–1227, https://doi.org/10.1175/1520-0469(1983)040<1218:TKOOAD>2.0.CO;2.

Marwitz, J. D., 1987: Deep Orographic Storms over the Sierra Nevada. Part I: Thermodynamic and Kinematic Structure. *J. Atmos. Sci.*, **44**, 159–173, https://doi.org/10.1175/1520-0469(1987)044<0159:DOSOTS>2.0.CO;2.

Massmann, A. K., J. R. Minder, R. D. Garreaud, D. E. Kingsmill, R. A. Valenzuela, A. Montecinos, S. L. Fults, and J. R. Snider, 2017: The Chilean Coastal Orographic

Accepted for publication in *Journal of the Atmospheric Sciences*. DOI 10.1175/JAS-D-21-0091.1.

887 Precipitation Experiment: Observing the Influence of Microphysical Rain Regimes on
888 Coastal Orographic Precipitation. *J. Hydrometeor.*, **18**, 2723–2743,
889 https://doi.org/10.1175/JHM-D-17-0005.1.
890 McFarquhar, G. M., J. A. Finlon, D. M. Stechman, W. Wu, R. C. Jackson, and M. Freer, 2018:
891 University of Illinois/Oklahoma Optical Array Probe (OAP) Processing Software,
892 https://doi.org/10.5281/ZENODO.1285969.
893 McMurdie, L. A., A. K. Rowe, R. A. Houze, S. R. Brodzik, J. P. Zagrodnik, and T. M. Schuldt,
894 2018: Terrain- Enhanced Precipitation Processes Above the Melting Layer: Results From
895 OLYMPEX. *J. Geophys. Res. Atmos.*, **123**, https://doi.org/10.1029/2018JD029161.
896 Medina, S., B. F. Smull, R. A. Houze, and M. Steiner, 2005: Cross-Barrier Flow during
897 Orographic Precipitation Events: Results from MAP and IMPROVE. *J. Atmos. Sci.*, **62**,
898 3580–3598, https://doi.org/10.1175/JAS3554.1.
899 Medina, S., E. Sukovich, and R. A. Houze, 2007: Vertical Structures of Precipitation in Cyclones
900 Crossing the Oregon Cascades. *Mon. Wea. Rev.*, **135**, 3565–3586,
901 https://doi.org/10.1175/MWR3470.1.
902 Mesinger, F., and Coauthors, 2006: North American Regional Reanalysis. *Bull. Amer. Meteor.*
903 *Soc.*, **87**, 343–360, https://doi.org/10.1175/BAMS-87-3-343.
904 Minder, J. R., D. R. Durran, and G. H. Roe, 2011: Mesoscale Controls on the Mountainside
905 Snow Line. *J. Atmos. Sci.*, **68**, 2107–2127, https://doi.org/10.1175/JAS-D-10-05006.1.
906 Moisseev, D., E. Saltikoff, and M. Leskinen, 2009: Dual-Polarization Weather Radar
907 Observations of Snow Growth Processes. *Vol. 13B.2 of 34th Conf. on Radar Meteor.*,
908 Williamsburg, VA, Amer. Meteor. Soc., https://ams.confex.com/
909 ams/pdfpapers/156123.pdf.

910 Petersen, W. A., R. A. Houze, and L. A. McMurdie, 2018: GPM Ground Validation OLYMPEX
911 Field Campaign Data Collection. Data set available online http://ghrc.nsstc.nasa.gov/
912 from the NASA EOSDIS Global Hydrology Resource Center Distributed Active Archive
913 Center Huntsville, Alabama, U.S.A.
914 https://doi.org/10.5067/GPMGV/OLYMPEX/DATA101.
915 Petersen, W. A., A. Tokay, P. N. Gatlin, and M. T. Wingo, 2017a: GPM Ground Validation
916 Autonomous Parsivel Unit (APU) OLYMPEX [Subsets used: APU03, APU06, APU08].
917 Dataset available online from the NASA Global Hydrology Resource Center DAAC,
918 Huntsville, Alabama, U.S.A.
919 https://doi.org/10.5067/GPMGV/OLYMPEX/APU/DATA301.
920 Petersen, W. A., D. B. Wolff, J. Wang, and A. Tokay, 2017b: GPM Ground Validation Met One
921 Rain Gauge Pairs OLYMPEX [Subsets used: Fishery site, Prairie Creek site, Wynoochee
922 site]. Dataset available online from the NASA Global Hydrology Resource Center
923 DAAC, Huntsville, Alabama, U.S.A.
924 https://doi.org/10.5067/GPMGV/OLYMPEX/GAUGES/DATA201.
925 Petty, G. W., and W. Huang, 2011: The Modified Gamma Size Distribution Applied to
926 Inhomogeneous and Nonspherical Particles: Key Relationships and Conversions. *J.*
927 *Atmos. Sci.*, **68**, 1460–1473, https://doi.org/10.1175/2011JAS3645.1.
928 Pippitt, J. L., D. B. Wolff, W. A. Petersen, and D. A. Marks, 2015: Data and Operational
929 Processing for NASA's GPM Ground Validation Program. *37th Conf. Radar Meteor.*,
930 Norman, OK. Amer. Meteor. Soc. https://ams.confex.
931 com/ams/37RADAR/webprogram/Paper275627.html.

Accepted for publication in *Journal of the Atmospheric Sciences*. DOI 10.1175/JAS-D-21-0091.1.

Poellot, M. R., A. J. Heymsfield, and A. Bansemer, 2017: GPM Ground Validation UND Citation Cloud Microphysics OLYMPEX. Dataset available online from the NASA Global Hydrology Resource Center DAAC, Huntsville, Alabama, U.S.A. https://doi.org/10.5067/GPMGV/OLYMPEX/MULTIPLE/DATA201.

Roe, G. H., 2005: Orographic Precipitation. *Annu. Rev. Earth Planet. Sci.*, **33**, 645–671, https://doi.org/10.1146/annurev.earth.33.092203.122541.

Rutledge, S. A., K. Young, H. Voemel, D. Hudak, and P. Rodriguez, 2018: GPM Ground Validation Upper Air Radiosonde OLYMPEX. https://doi.org/10.5067/GPMGV/OLYMPEX/RADIOSONDES/DATA101.

Ryzhkov, A. V., 2007: The Impact of Beam Broadening on the Quality of Radar Polarimetric Data. *J. Atmos. Oceanic Technol.*, **24**, 729–744, https://doi.org/10.1175/JTECH2003.1.

Sánchez-Diezma, R., I. Zawadzki, and D. Sempere-Torres, 2000: Identification of the bright band through the analysis of volumetric radar data. *J. Geophys. Res.*, **105**, 2225–2236, https://doi.org/10.1029/1999JD900310.

Schrom, R. S., and M. R. Kumjian, 2016: Connecting Microphysical Processes in Colorado Winter Storms with Vertical Profiles of Radar Observations. *J. Appl. Meteor. Climatol.*, **55**, 1771–1787, https://doi.org/10.1175/JAMC-D-15-0338.1.

Schrom, R. S., M. R. Kumjian, and Y. Lu, 2015: Polarimetric Radar Signatures of Dendritic Growth Zones within Colorado Winter Storms. *J. Appl. Meteor. Climatol.*, **54**, 2365–2388, https://doi.org/10.1175/JAMC-D-15-0004.1.

Smith, R. B., 1979: The Influence of Mountains on the Atmosphere. *Adv. Geophys.*, Vol. 21, Academic Press, 87–230, https://doi.org/10.1016/S0065-2687(08)60262-9.

Accepted for publication in *Journal of the Atmospheric Sciences*. DOI 10.1175/JAS-D-21-0091.1.

954 Viviroli, D., H. H. Dürr, B. Messerli, M. Meybeck, and R. Weingartner, 2007: Mountains of the
955 world, water towers for humanity: Typology, mapping, and global significance. *Water*
956 *Resour. Res*., **43**, https://doi.org/10.1029/2006WR005653.
957 White, A. B., D. J. Gottas, E. T. Strem, F. M. Ralph, and P. J. Neiman, 2002: An Automated
958 Brightband Height Detection Algorithm for Use with Doppler Radar Spectral Moments.
959 *J. Atmos. Oceanic Technol.*, **19**, 687–697, https://doi.org/10.1175/1520-
960 0426(2002)019<0687:AABHDA>2.0.CO;2.
961 White, A. B., P. J. Neiman, F. M. Ralph, D. E. Kingsmill, and P. O. Persson, 2003: Coastal
962 Orographic Rainfall Processes Observed by Radar during the California Land-Falling Jets
963 Experiment. *J. Hydrometeor.*, **4**, 264–282, https://doi.org/10.1175/1525-
964 7541(2003)4<264:CORPOB>2.0.CO;2.
965 Wolff, D. B., D. A. Marks, and W. A. Petersen, 2015: General Application of the Relative
966 Calibration Adjustment (RCA) Technique for Monitoring and Correcting Radar
967 Reflectivity Calibration. *J. Atmos. Oceanic Technol.*, **32**, 496–506,
968 https://doi.org/10.1175/JTECH-D-13-00185.1.
969 Wolff, D. B., D. A. Marks, W. A. Petersen and J. L. Pippitt, 2017: GPM Ground Validation
970 NASA S-Band Dual Polarimetric (NPOL) Doppler Radar OLYMPEX. Dataset available
971 online from the NASA Global Hydrology Resource Center DAAC, Huntsville, Alabama,
972 U.S.A. https://doi.org/10.5067/GPMGV/OLYMPEX/NPOL/DATA301.
973 Zagrodnik, J. P., L. A. McMurdie, and R. A. Houze, 2018: Stratiform Precipitation Processes in
974 Cyclones Passing over a Coastal Mountain Range. *J. Atmos. Sci.*, **75**, 983–1004,
975 https://doi.org/10.1175/JAS-D-17-0168.1.

Accepted for publication in *Journal of the Atmospheric Sciences*. DOI 10.1175/JAS-D-21-0091.1.

Zagrodnik, J. P., L. A. McMurdie, R. A. Houze, and S. Tanelli, 2019: Vertical Structure and Microphysical Characteristics of Frontal Systems Passing over a Three-Dimensional Coastal Mountain Range. *J. Atmos. Sci.*, **76**, 1521–1546, https://doi.org/10.1175/JAS-D-18-0279.1.

Zagrodnik, J. P., L. McMurdie, and R. Conrick, 2021: Microphysical Enhancement Processes within Stratiform Precipitation on the Barrier and Sub-Barrier Scale of the Olympic Mountains. *Mon. Wea. Rev.*, https://doi.org/10.1175/MWR-D-20-0164.1.

995 FIGURES

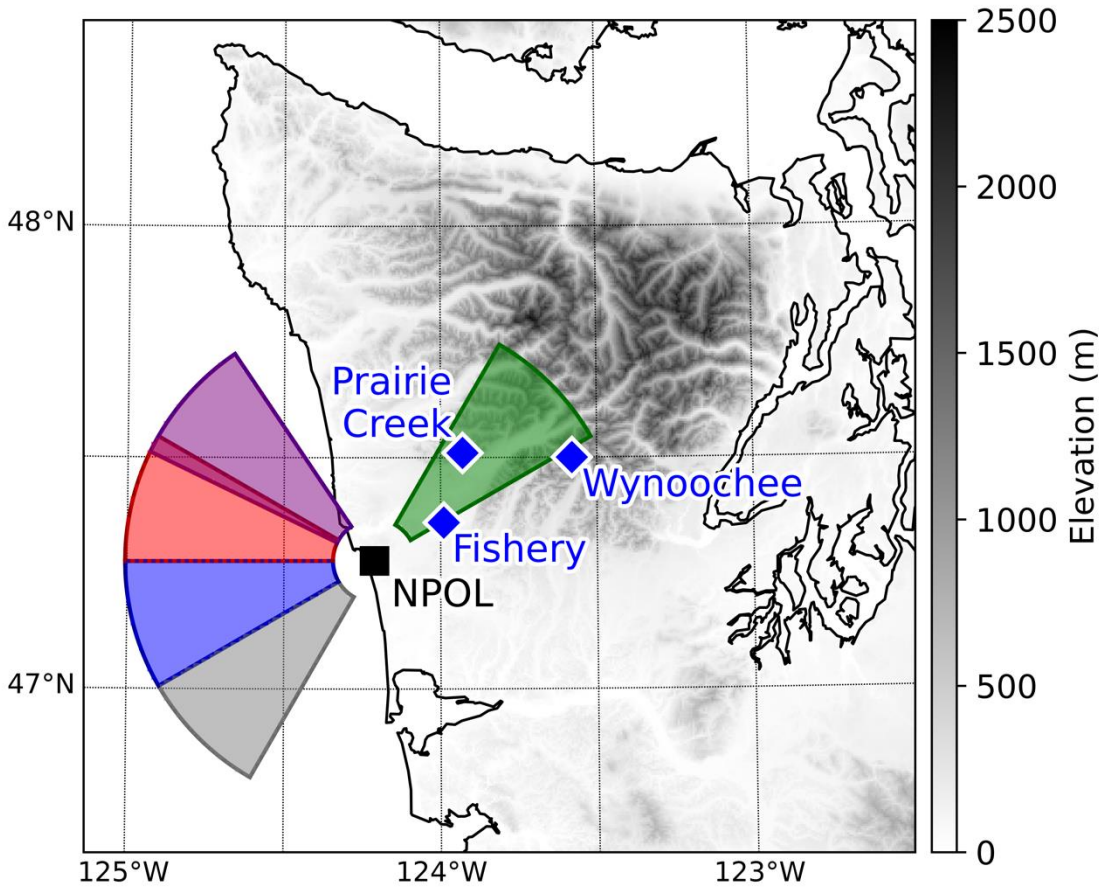

996

997 Figure 1. Map of the Olympic Peninsula showing the position of the NASA S-band dual-
998 polarization Doppler radar (NPOL, 139 m) and three ground sites (Fishery, 52 m; Prairie Creek,
999 543 m; Wynoochee, 1,018 m) on the windward slopes. Terrain elevation is shown in the gray
1000 shading. Colored regions indicate radar sectors of 10 to 60 km radial range: southwest, gray;
1001 south-southwest, blue; north-northwest, red; northwest, violet; northeast, green.

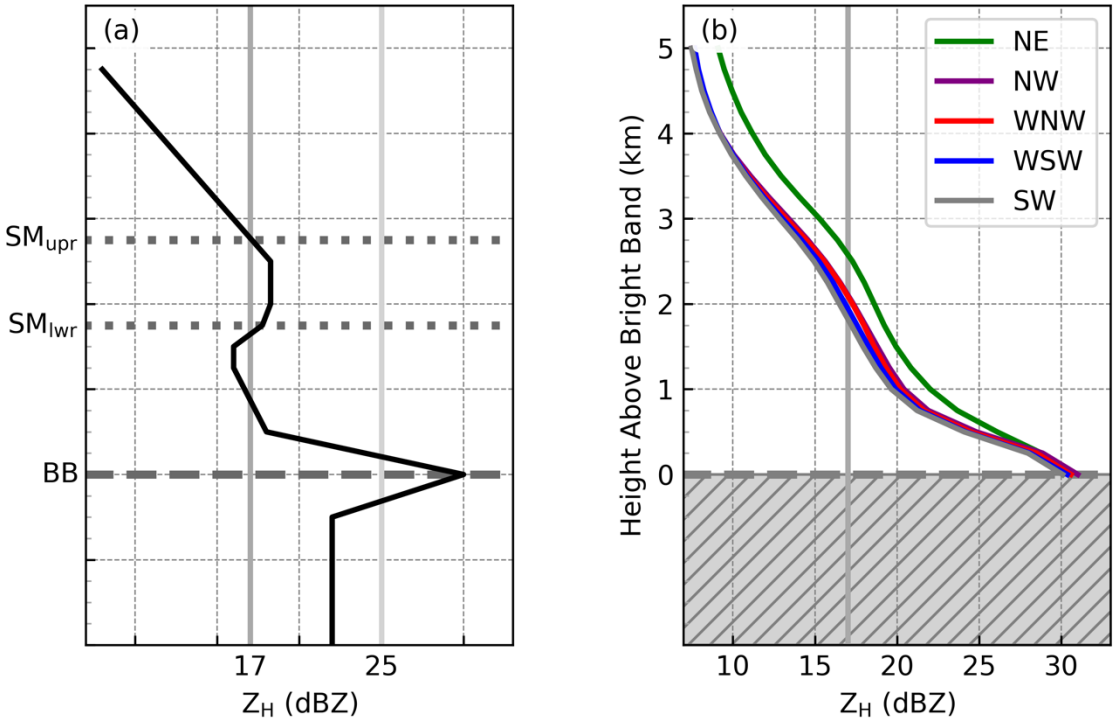

1002

1003 Figure 2. Vertical profiles of Z_H illustrating (a) a schematic diagram of the bright band (BB) and
1004 secondary Z_H maximum (SM) features in a vertical column at a single grid point and (b) radar
1005 sector composite profiles from all NPOL scan cycles having a bright band. In the schematic (a), a
1006 light gray vertical line highlights the 25 dBZ threshold used to define a bright band and a dark
1007 gray vertical line highlights the 17 dBZ threshold used for detection of a secondary Z_H maximum
1008 layer. The lower extent of the secondary Z_H maximum layer, SM_{lwr}, is defined by the initial level
1009 of increase in Z_H with height above the bright band. The upper extent of the secondary Z_H
1010 maximum layer, SM_{upr}, is the uppermost level having a Z_H value greater than the level
1011 immediately below SM_{lwr}. Composite profiles (b) were adjusted to be bright band relative prior
1012 to averaging.

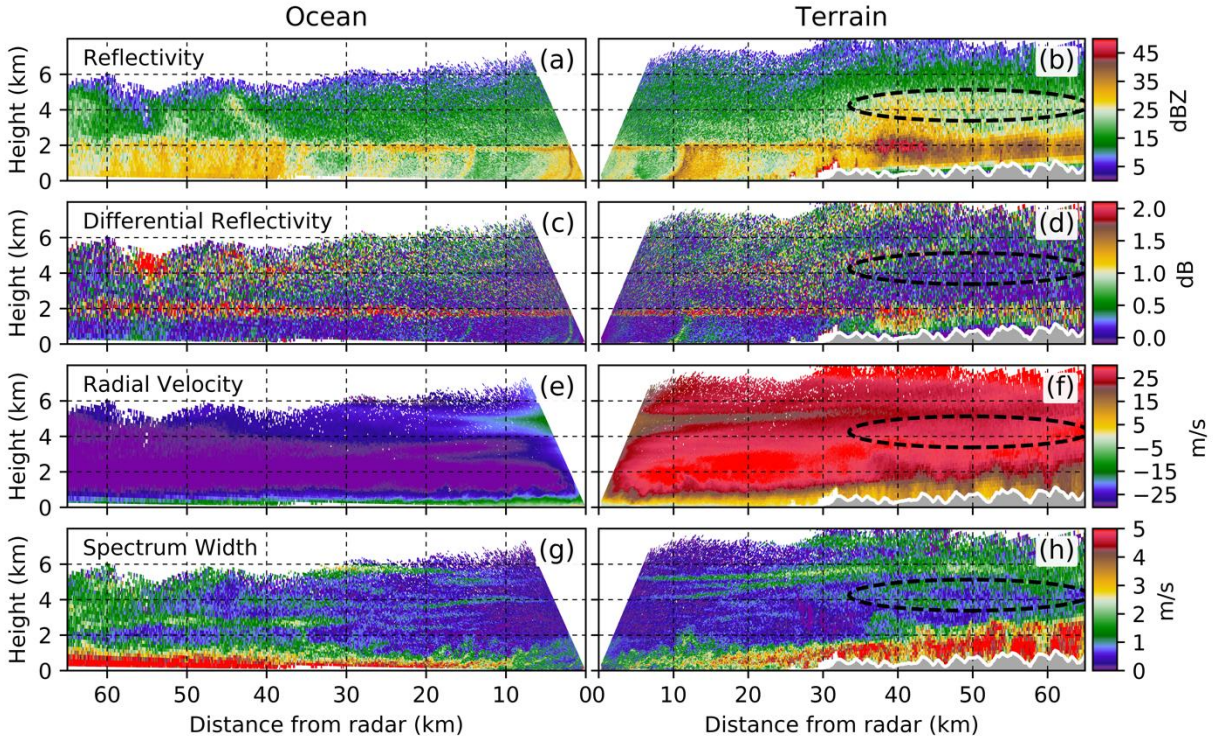

1013

1014 Figure 3. RHI scans from NPOL for (a, b) reflectivity, (c, d) differential reflectivity, (e, f) radial
1015 velocity, and (g, h) spectrum width. The RHI scans occurred at (a, c, e, g) 1441 UTC 03
1016 December 2015 at an azimuthal angle of 219° over the upstream ocean and at (b, d, f, h) 1453
1017 UTC 03 December 2015 at an azimuthal angle of 38° over the windward terrain of the Olympic
1018 Mountains. The black dashed ellipse (b, d, f, h) represents the approximate location of the
1019 secondary Z_H maximum layer. Gray shaded regions depict the terrain of the Olympic Mountains.

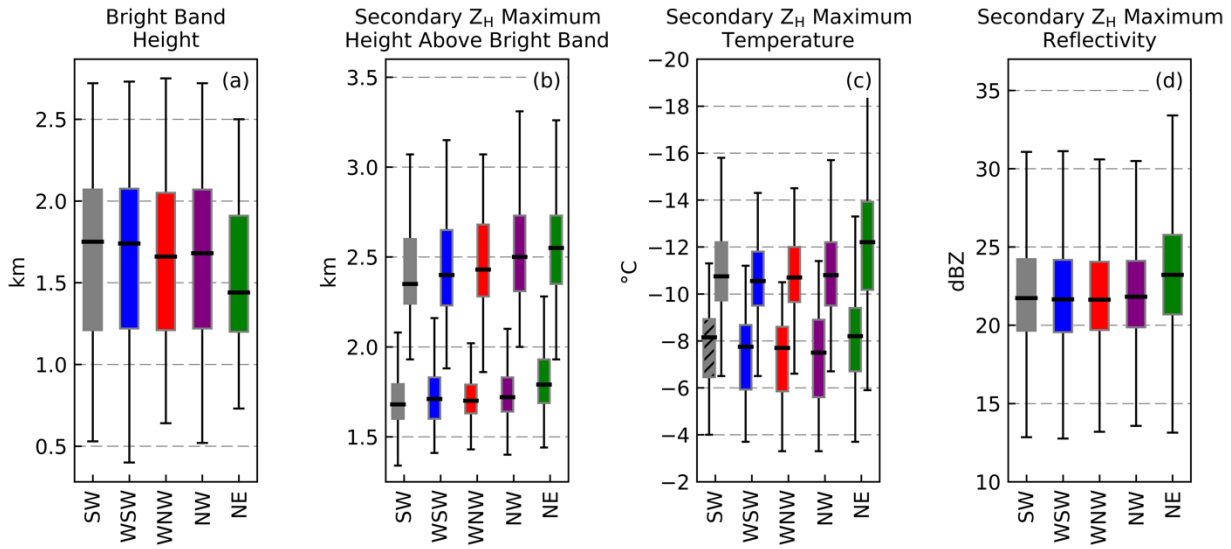

Figure 4. NPOL radar sector distributions of (a) bright band height, (b) secondary Z_H maximum lower and upper extent heights above the bright band, (c) secondary Z_H maximum lower and upper extent temperatures, and (d) column-averaged Z_H values from grid points with a secondary Z_H maximum. The box represents the 25th and 75th percentiles and the whiskers are the 5th and 95th percentiles of the distributions. The dark horizontal lines are the median values. Hatching in the color fill indicates that the ocean-focused distribution was not statistically significantly different from the terrain-focused distribution based on a two-tailed t-test at a 95% significance level.

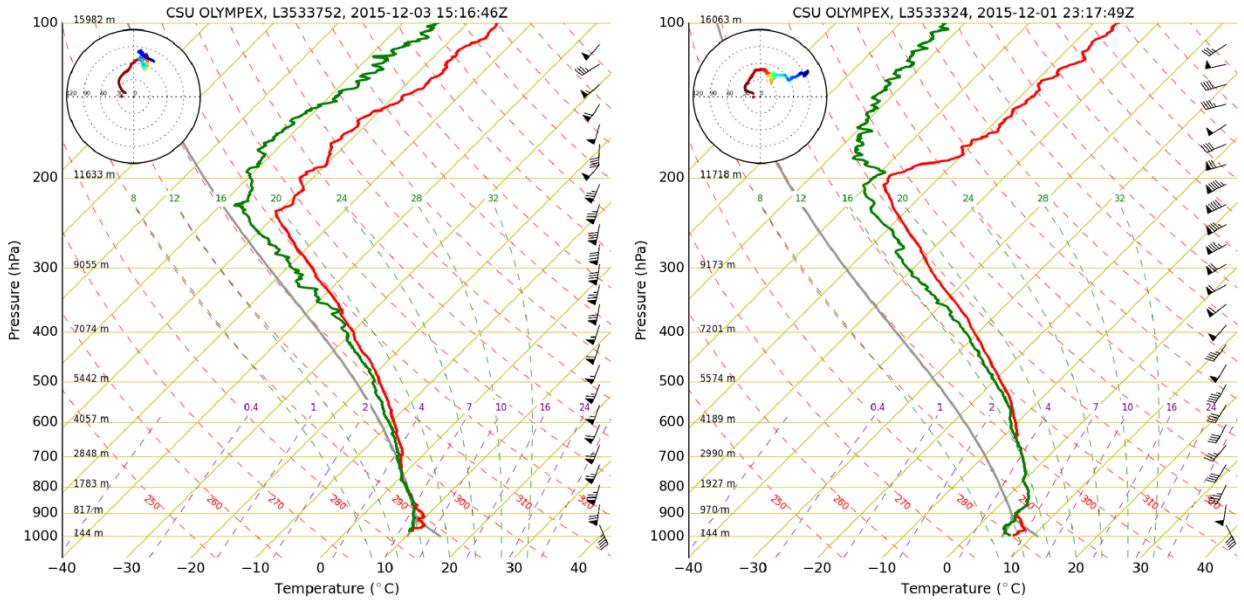

1029

1030 Figure 5. Skew-T log-P diagrams of temperature (red) and dew point temperature (green) from

1031 atmospheric soundings launched at the NPOL site at (left) 1516 UTC 03 December 2015 and

1032 (right) 2317 01 December 2015. Figures obtained from

1033 http://olympex.atmos.washington.edu/index.html?x=OLYMPEX_Obs

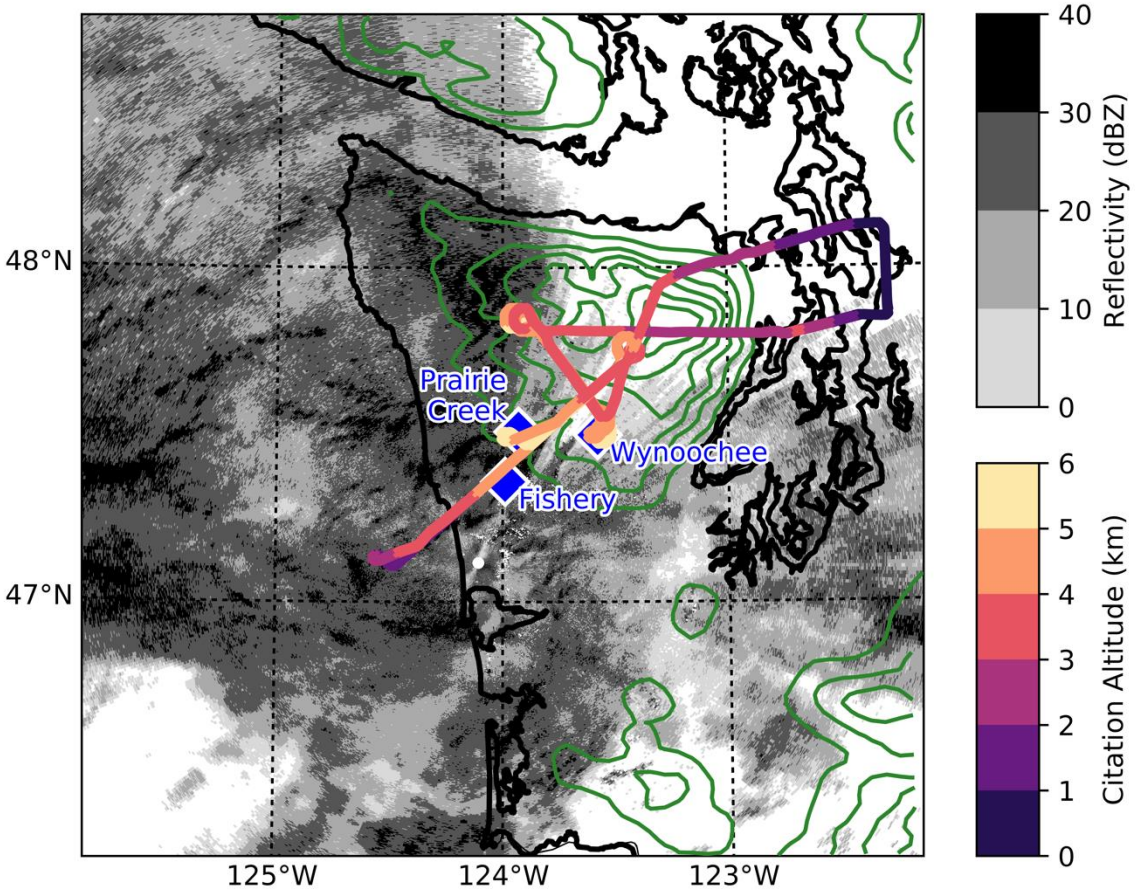

1034

1035 Figure 6. Flight track between approximately 1400 and 1700 UTC on 03 December 2015 with
1036 altitude in km indicated by color shading. Grayscale shading is the reflectivity field of the lowest
1037 level (0.5°) plan position indicator (PPI) scan between 1447 and 1452 UTC 03 December 2015
1038 from the coastal KLGX WSR-88D radar at Langley Hill, WA. Blue diamonds indicate the three
1039 ground sites used in this study. Green contours depict the terrain elevation at 250 m intervals
1040 beginning at 250 m.

Accepted for publication in *Journal of the Atmospheric Sciences*. DOI10.1175/JAS-D-21-0091.1.

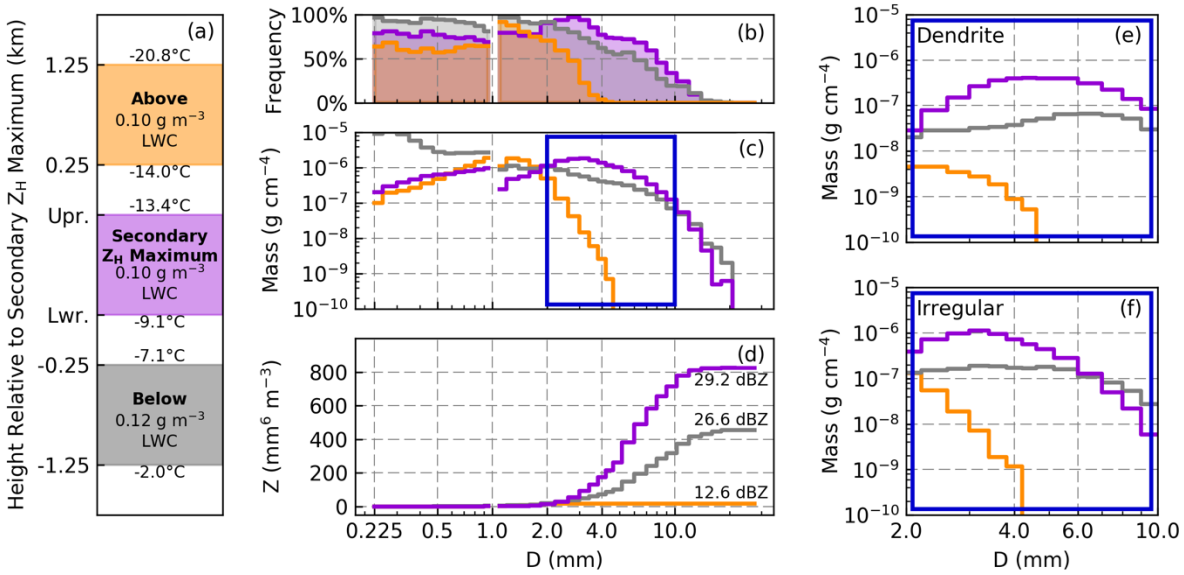

1041

1042 Figure 7. In situ measurements on 03 December 2015 within the secondary Z_H maximum layer
1043 (violet), within a 1 km deep layer above (orange), and within a 1 km deep layer below (gray)
1044 separated by 250 m. (a) Schematic depicting each layer with temperature ranges obtained from
1045 the 1516 UTC 03 December 2015 sounding and mean LWCs from King probe measurements
1046 exceeding 0.05 g m^{-3}. (b) Histograms of the frequency of occurrence of particles by diameter, (c)
1047 flight-averaged PSDs, and (d) cumulative reflectivity by particle size constructed from 2D-S
1048 (0.225 to 1 mm) and HVPS-3 (1 to 32.5 mm) measurements. Habit specific PSDs for (e)
1049 dendritic and (f) irregular particles from 2 to 10 mm corresponding to the blue boxed region in
1050 panel (c).

Accepted for publication in *Journal of the Atmospheric Sciences*. DOI10.1175/JAS-D-21-0091.1.

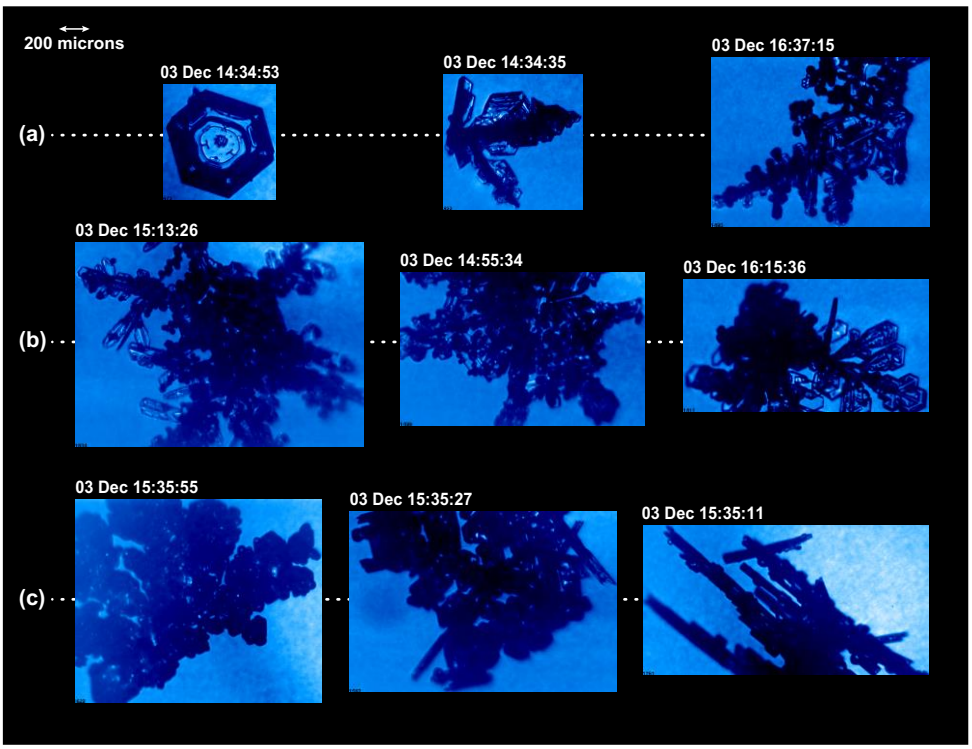

1051

1052 Figure 8. In situ Cloud Particle Imager example imagery from (a) above, (b) within, and (c)

1053 below the secondary Z_H maximum layers on 03 December 2015.

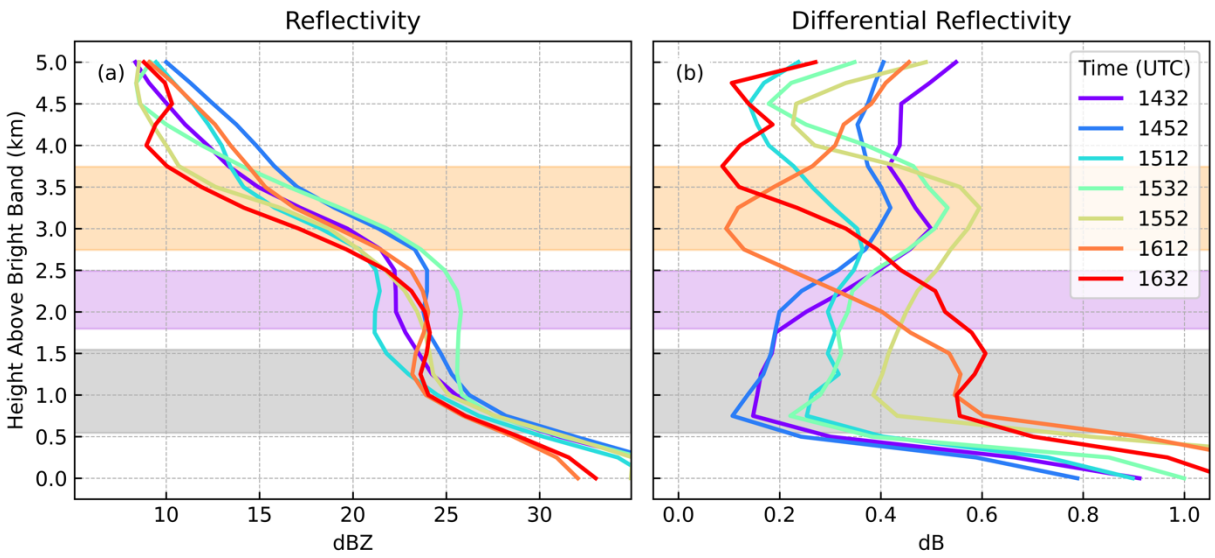

Figure 9. Bright-band relative vertical profiles of (a) reflectivity and (b) differential reflectivity from NPOL terrain-focused radar scan cycles coinciding with the 03 December 2015 flight. Shaded regions represent the position of the secondary Z_H maximum layer and the 1 km layers above and below colored according to the schematic in Fig. 7a. Layer heights are an average over all radar scan cycles.

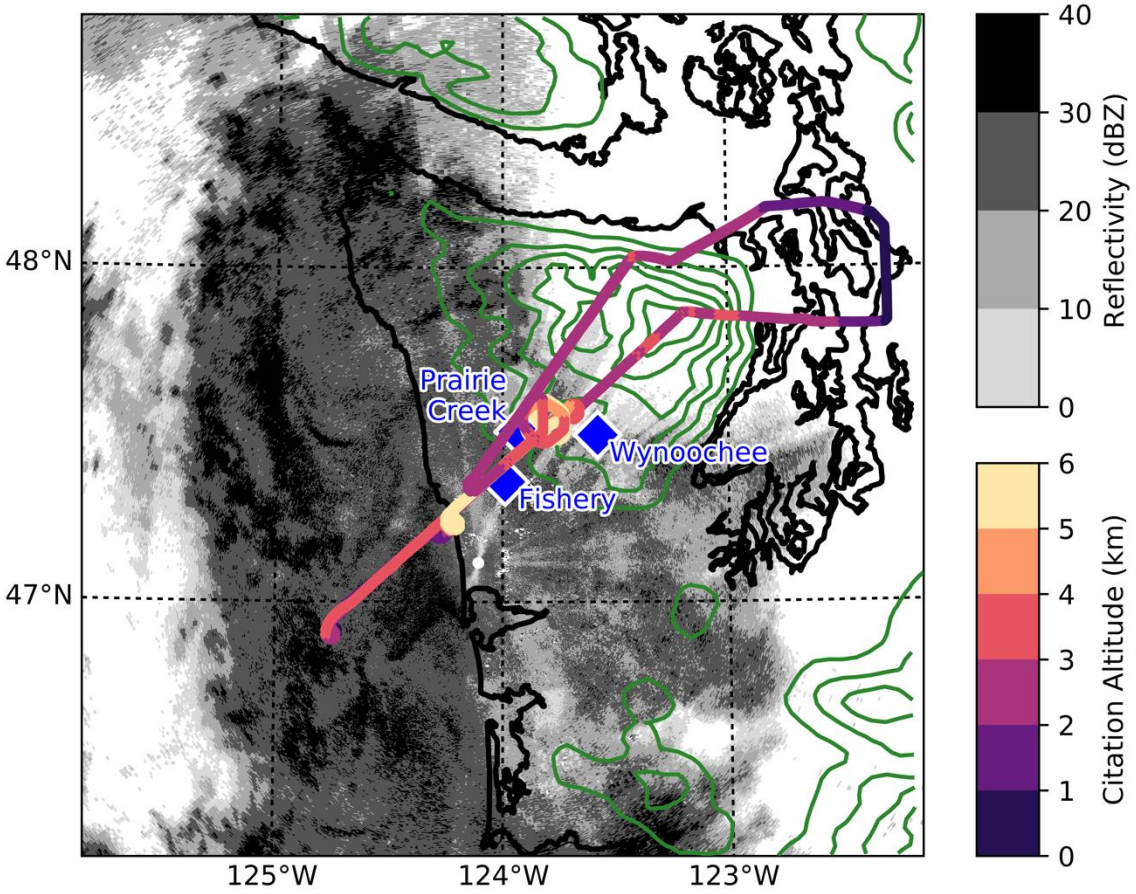

1061

1062 Figure 10. As in Figure 6, but for the flight between approximately 2300 UTC 01 to 0200 UTC

1063 02 December 2015. The KLGX PPI scan is for 2307-2312 UTC 01 December 2015.

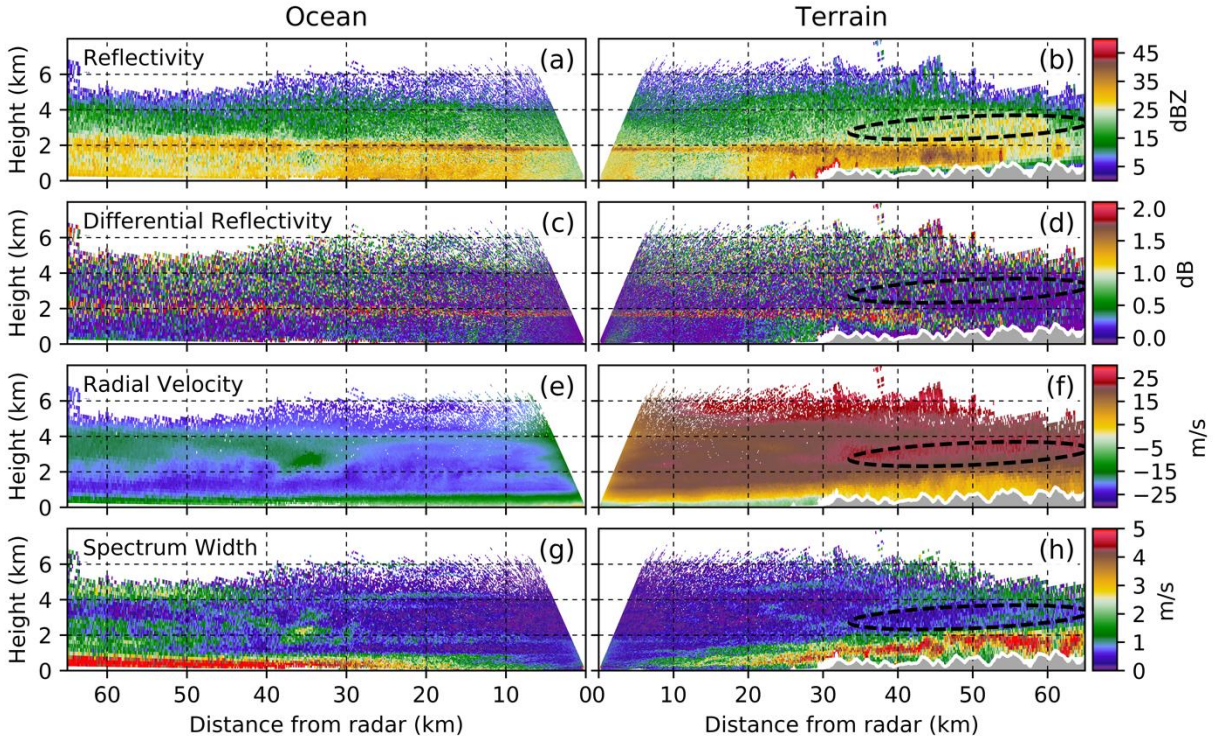

1064

1065 Figure 11. As in Figure 3, but for RHI scans at (a, c, e, g) 2301 UTC and (b, d, f, h) 2313 UTC

1066 on 01 December 2015.

1067

1068

1069

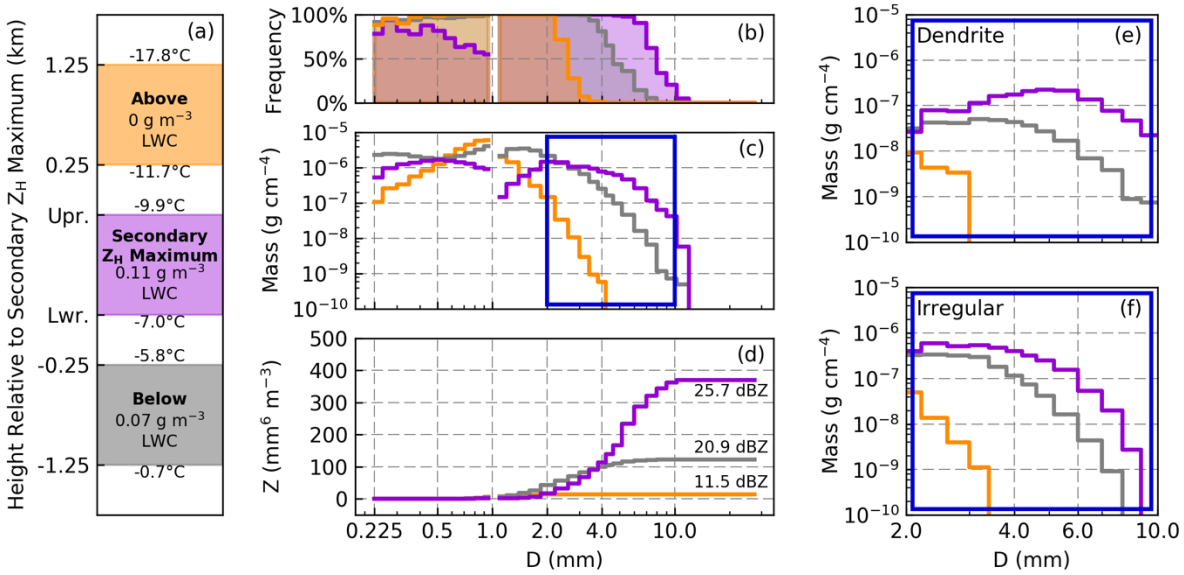

Figure 12. As in Figure 7 but for the 01-02 December 2015 flight. Temperature ranges for each layer shown in panel (a) were obtained from the 2317 UTC 01 December 2015 sounding.

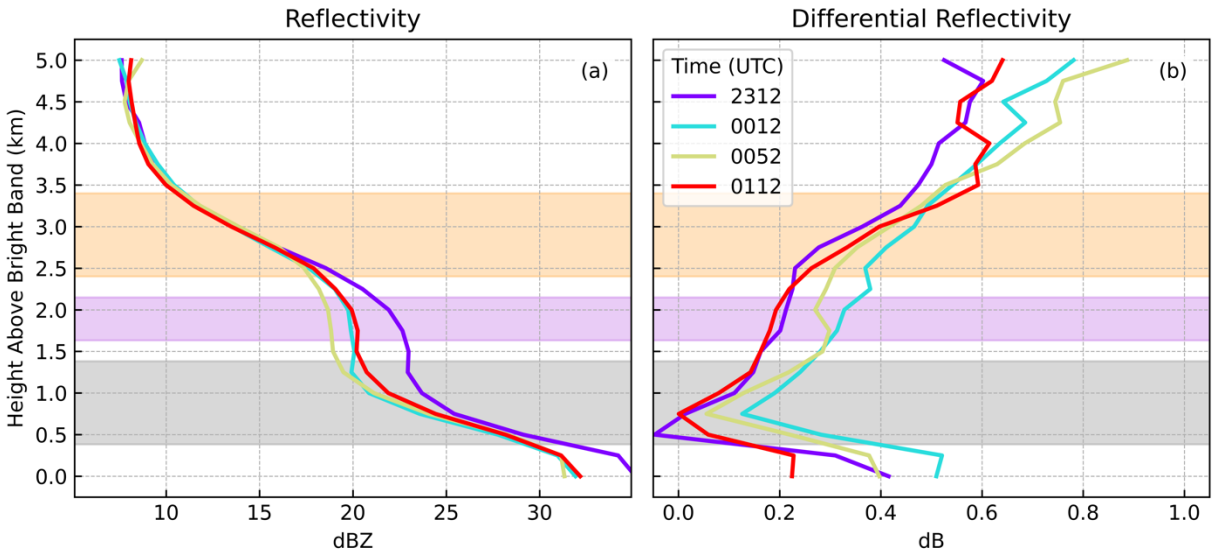

1079

1080 Figure 13. As in Figure 9, but for 01-02 December 2015.

1081

Accepted for publication in *Journal of the Atmospheric Sciences*. DOI10.1175/JAS-D-21-0091.1.

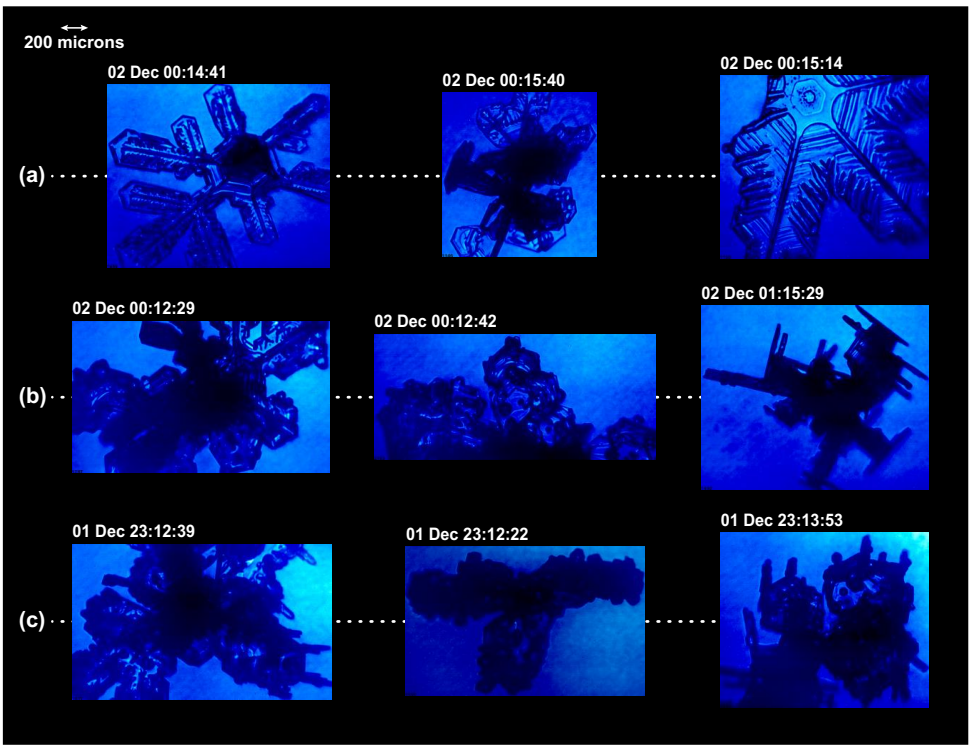

1082

1083 Figure 14. As in Figure 8, but for 01-02 December 2015.

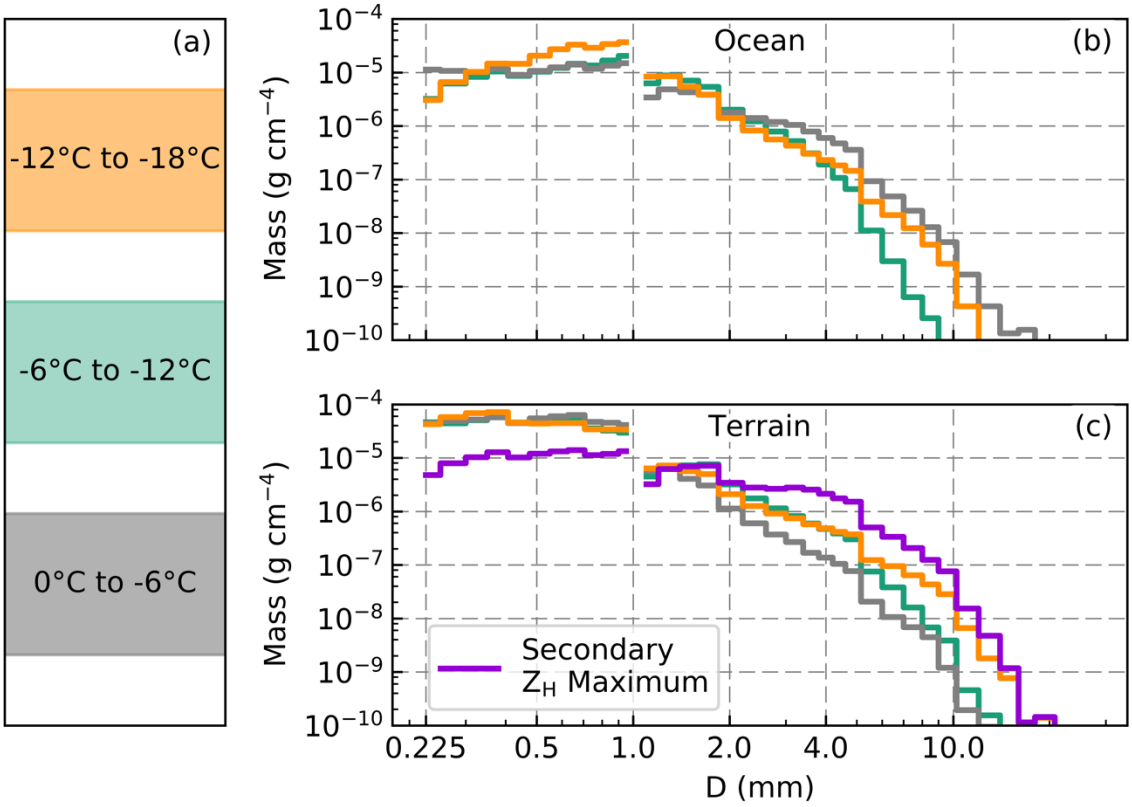

1084

1085 Figure 15. Average PSDs derived from 2D-S and HVPS-3 measurements on all flights. (a)
1086 Temperature ranges of bright-band-only period observations comparable to above (orange),
1087 within (green), and below (gray) secondary Z_H maximum layers. (b) PSDs derived from flights
1088 over the upstream ocean. (c) PSDs derived from flights over the terrain with violet corresponding
1089 to the secondary Z_H maximum layer. Observations from the 18 December 2015 were not used in
1090 the 0°C to -6°C calculations due to sampling at the bright band.

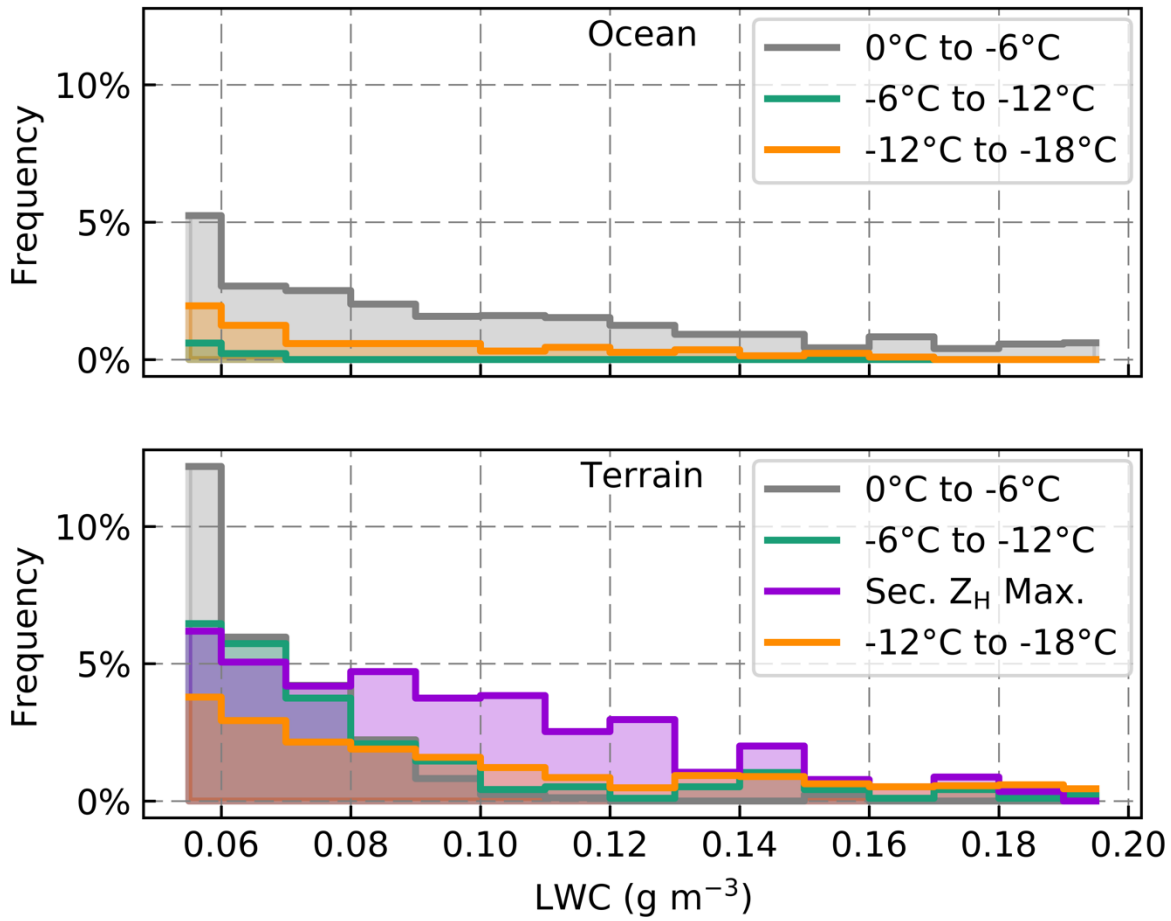

Figure 16. Histograms of LWC measurements greater than 0.05 g m^{-3} from the King probe by layer as in Fig. 15a during all bright-band-only periods over the upstream ocean (top) and over the terrain (bottom). The violet histogram over the terrain corresponds to measurements from the secondary reflectivity Z_H maximum layer.

Accepted for publication in *Journal of the Atmospheric Sciences*. DOI10.1175/JAS-D-21-0091.1.

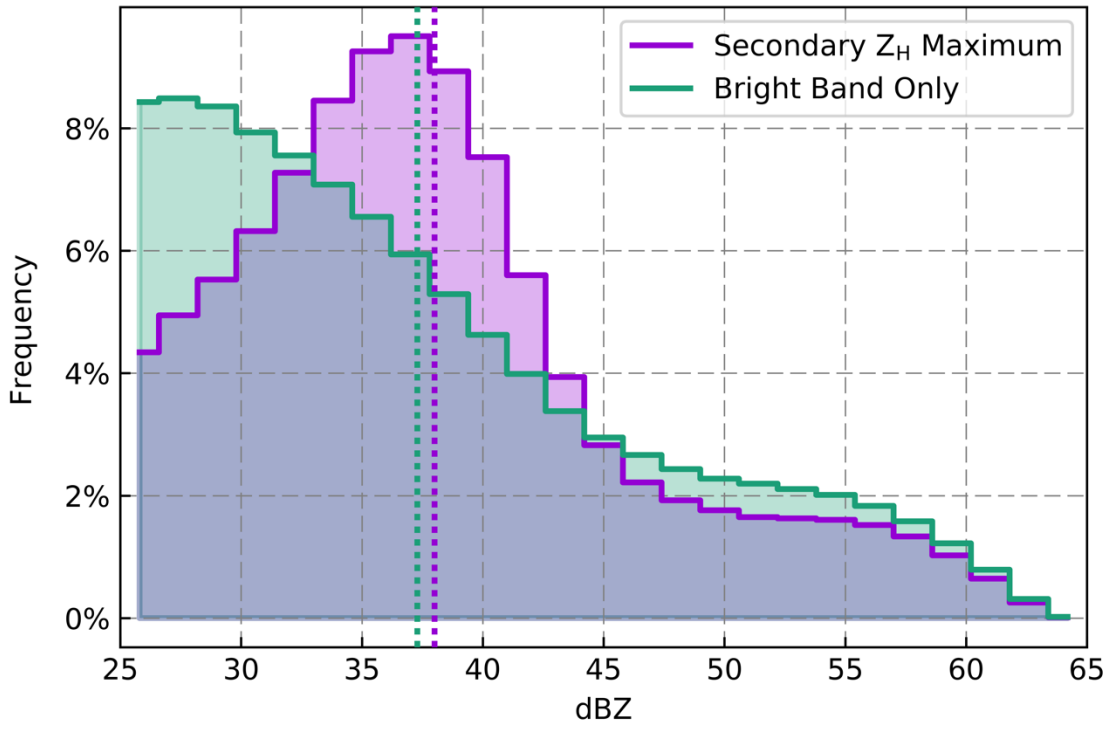

1096

1097 Figure 17. Histograms of Z_H at the bright band from individual grid points within the terrain-

1098 focused radar sector during all secondary Z_H maxima (violet) and bright-band-only (green)

1099 periods. Dashed vertical lines indicate the mean values of the distribution.

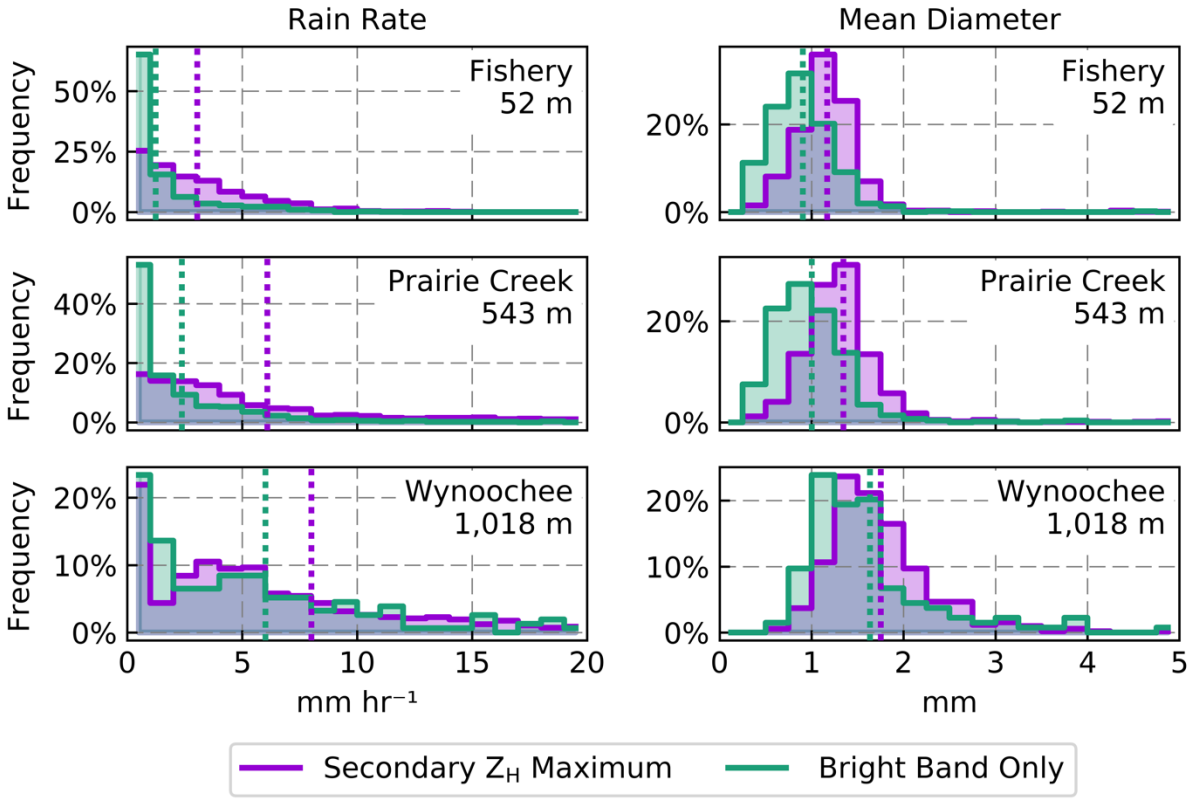

Figure 18. Histograms of rain rate and mass-weighted mean drop diameter from OLYMPEX Parsivel^2 disdrometer measurements during all secondary Z_H maximum (violet) and bright-band-only (green) periods at the three windward ground sites shown in Fig. 1. Dashed vertical lines indicate the mean values of each distribution.